Mon. Not. R. Astron. Soc. **308**, 180–200 (1999)

Measuring the three-dimensional shear from simulation data, with applications to weak gravitational lensing

H. M. P. Couchman,[1]★ Andrew J. Barber[2]★ and Peter A. Thomas[2]

[1]*Department of Physics and Astronomy, University of Western Ontario, London, Ontario N6A 3K7, Canada*
[2]*Astronomy Centre, University of Sussex, Falmer, Brighton BN1 9QJ*

Accepted 1999 April 1. Received 1999 February 24; in original form 1998 October 5

ABSTRACT

We have developed a new three-dimensional algorithm, based on the standard P^3M method, for computing deflections resulting from weak gravitational lensing. We compare the results of this method with those of the two-dimensional planar approach, and rigorously outline the conditions under which the two approaches are equivalent. Our new algorithm uses a Fast Fourier Transform convolution method for speed, and has a variable softening feature to provide a realistic interpretation of the large-scale structure in a simulation. The output values of the code are compared with those from the Ewald summation method, which we describe and develop in detail. With an optimal choice of the high-frequency filtering in the Fourier convolution, the maximum errors, when using only a single particle, are about 7 per cent, with an rms error less than 2 per cent. For ensembles of particles, used in typical *N*-body simulations, the rms errors are typically 0.3 per cent. We describe how the output from the algorithm can be used to generate distributions of magnification, source ellipticity, shear and convergence for large-scale structure.

Key words: methods: numerical – galaxies: clusters: general – cosmology: miscellaneous – gravitational lensing – large-scale structure of Universe.

1 INTRODUCTION

Procedures for the generation of cosmological *N*-body simulations have become increasingly sophisticated in recent years. We have now developed an algorithm for assessing in great detail, and with considerable speed and accuracy, the effects of the large-scale mass distributions within these simulations on the passage of light from sources at great distances.

Our algorithm computes the nine components in three dimensions of the second derivative of the gravitational potential at a large number of locations within the volume of *N*-body particle simulations. We refer to these components quite generally, throughout this paper, as the three-dimensional shear matrix, or individually as the shear components or values. However, in the analysis of the computed data, for which the effects of lensing along a particular line of sight are required, the two-dimensional 'effective lensing potentials' (see Section 5.3) are generated by integrating the three-dimensional components along the line of sight. These effective lensing potentials are used to construct the Jacobian matrix (defined in Section 5.3), which is recursively generated along the line of sight, and from the final Jacobian matrix the magnifications and two-dimensional shear, which are defined in Section 5.3, may be determined.

★ E-mail: couchman@coho.astro.uwo.ca (HMPC); abarber@star.cpes.susx. ac.uk (AJB)

1.1 Previous work

There are numerous methods for studying the 'weak' gravitational lensing due to large-scale structure, the most common being 'ray-tracing,' in which individual light rays are traced backwards from the observer, and the deflections occuring at each lens-plane are calculated. The lens-planes are two-dimensional projections of the mass content within a small redshift interval, usually equal to the simulation box depth.

Schneider & Weiss (1988b) have used this method by shooting, typically, 10^8 rays through the lens-planes to strike the source plane within a chosen square region, called the detection field. Each plane is divided into 51^2 pixels, typically, and the particles (stars in this case) are categorized as near or far for computational purposes. The deflection by stars further away than about 8 pixel dimensions from the centre of each pixel is approximated in a Taylor series, whilst the deflections due to the nearby stars are computed individually. The rays are shot through a cylinder with a radius such that the rays meet the source plane in or near the detection field. They claim that the resulting amplification factors are hardly affected by edge effects caused by strong lensing of

rays outside the shooting cylinder, but which might strike the detection field. The amplification factors are determined directly from the mapping of the rays on to the pixels of the detection field.

Jaroszyński et al. (1990) evaluate the matter column density in a matrix of pixels for each of the lens-planes, based on their simulation boxes. By making use of the periodicity in the particle distribution orthogonal to the line of sight, they are able to arrange for each ray traced to be centralized within planes of one full period in extent. In this way, the deflections on each ray take account of all the matter within one complete period. They calculate, not deflection angles, but the two two-dimensional components of the shear (see Section 5.3), as ratios of the mean convergence of the beam. To do this, they assume that the matter in each of the 128^3 pixels resides at the centre point of each pixel. To follow the shearing across subsequent planes, they recursively generate the developing Jacobian matrix for each ray, in accordance with the multiple lens-plane theory (see Section 5.3).

Wambsganss (1990) uses the 'ray-tracing' method to study microlensing, Wambsganss, Cen & Ostriker (1998) use it with cosmological *N*-body simulations, and Wambsganss et al. (1997) use the method for studying the dispersion in type Ia supernovæ. They randomly orient each simulation box, and project the matter contained within each on to a plane divided into pixels. They choose the central $8\,h^{-1}$ Mpc $\times$ $8\,h^{-1}$ Mpc region through which to shoot rays, (h is the Hubble constant in units of $100\,\mathrm{km\,s^{-1}}$ Mpc^{-1}), but account for the deflections of the rays in terms of all the matter in the plane of $80\,h^{-1}$ Mpc $\times$ $80\,h^{-1}$ Mpc. However, to speed up the computation, a hierarchical tree code in two dimensions is used to collect together those lenses (pixels) far away, whilst treating nearby lenses individually. The matter in each pixel, which measures $10\,h^{-1}$ kpc $\times$ $10\,h^{-1}$ kpc, is assumed to be uniformly spread. The multiple lens-plane theory (see Section 5.3) is used for large numbers of rays to compute the mappings of images and sources, the distribution of magnifications, and statistics of angular separations of multiple images.

Marri & Ferrara (1998) select a total of 50 planes, evenly spaced in redshift space, between redshifts of $z = 0$ and $z = 10$. Their two-dimensional matter distribution on each plane consists of point masses without softening, so that their approach produces very high magnifications (greater than 20) for each of their chosen cosmologies, using the 'ray-tracing' method.

Premadi, Martel & Matzner (1998) have used five different sets of initial conditions for each *N*-body cosmological simulation, so that the plane projections of each simulation box can be chosen randomly from any one of the five, and then randomly translated, using the periodic properties of each box. In this way they are able to avoid correlations in the large-scale structure between adjacent boxes. A considerable improvement to the 'ray-tracing' method has then been made. They solve the two-dimensional Poisson equation on a grid, and invert the equation using a two-dimensional Fast Fourier Transform (FFT) method to obtain the first and second derivatives of the gravitational potential on each plane. From these data, cumulative deflections and the developing Jacobian matrix can be obtained, which provides the data for determining overall magnifications.

An alternative to the conventional form of backwards 'ray-tracing' was introduced by Refsdal (1970), who used a forwards 'ray-tracing' method with calculations of the differential deflection of light rays around a central ray to determine the distribution of magnifications.

Fluke, Webster & Mortlock (1998, and in preparation) have developed the 'ray-bundle' method. The principle here is to trace the passage of a discrete bundle of light rays as it passes through the deflection planes. The advantage of this method is that it provides a direct comparison between the shape and size of the bundle at the observer and at the source plane, so that the magnification, ellipticity and rotation can be determined straighforwardly. They shoot large numbers of bundles through the planes to obtain the statistical distribution of magnifications in different cosmological models.

A novel approach to weak gravitational lensing has been used by Holz & Wald (1998). They lay down a set of spheres between the observer and source, each containing an individual probability distribution of matter, in which a 'Newtonianly perturbed' Robertson–Walker metric is used. A scalar potential, related to the density perturbations, can then be evaluated, and this allows integration along straight lines through each sphere, to determine the angular deviations and shear.

Tomita (1998a) evaluates the potential at some 3000 positions between the observer and a source at $z = 5$, by using the periodic properties of each simulation cube to position it such that each evaluation position is centrally placed in the appropriate cube. To trace the paths of the light rays, they solve the null-geodesic equations, and use an analytical expression to determine the average potential through the interval between each pair of evaluation positions.

1.2 Motivation

Our motivation for the development of an algorithm to apply in three dimensions has stemmed from concern with possible limitations in the two-dimensional planar approaches to weak gravitational lensing. We therefore considered the following.

First, we wanted to investigate rigorously the conditions for equivalence of results obtained from three-dimensional realizations and two-dimensional planar projections. We show in Appendix B that the two-dimensional shear values at a point in the planar projection of a mass distribution are equal to the integrated three-dimensional values along the line of sight through one period (or cube dimension), in general, only if the distribution of mass is periodic along the line of sight, and the angular diameter distances through the depth of one period are assumed to be constant.

Secondly, we wanted a method which would unambiguously provide accurate values for the shear components, as if the contribution from all matter, effectively stretching to infinity, was included. Errors may occur in other methods if the contribution from matter within only a finite radius of the evaluation position is counted. For example, whilst Jaroszyński et al. (1990) include the matter contained within a plane of one complete period, Wambsganss (1990) and Wambsganss et al. (1997, 1998) introduce a slight bias, because rays near the edge of their shooting area are closer to the edge of the single period plane than rays near the centre of the shooting area. We investigate how quickly the shear component values converge to their true values, as increasing volumes of matter are included surrounding the evaluation position, and we report our findings in Section 4.

Thirdly, to achieve shear values consistent with those in a realistic universe, it is necessary to deal with the 'peculiar potential,' ϕ, which is related to the full gravitational potential, Φ, through the subtraction of a term depending upon the mean density. This approach, which we describe fully in Appendix A, ensures that we deal only with light-ray deflections arising from

departures from homogeneity; in a pure Robertson–Walker metric we would want no deflections. The approach is equivalent to requiring that the net total mass in the system be set to zero, so that for every mass there is a balancing uniform negative background mass. This net zero-mass requirement is achieved very simply in systems of particles which are periodically distributed in all dimensions, and we are therefore able to accommodate it easily in our algorithm.

Fourthly, we wanted to be able to apply our algorithm to cosmological simulations which were representative of the large-scale structure in the universe, rather than distributions of point masses. This has frequently been attempted by assuming each particle to be softened with the profile of an isothermal sphere. We wanted to improve on this by allowing the softening for each particle to reflect the environment in which it is located, so that large clusters and other dense structures dominate the light deflections, whilst the effects of isolated particles are minimized. This motivated us to consider the introduction of a variable softening facility to our algorithm.

Finally, a three-dimensional approach allows the use of the appropriate angular diameter distances at every single evaluation position within the three-dimensional realization. The two-dimensional methods discussed above necessarily assume that all the lensing mass within a given plane is at the same angular diameter distance, because the overall depth of the lens is considered to be small compared with the observer–lens, observer–source, and source–lens angular diameter distances. However, the depth of a single simulation cube employed in weak lensing (in our case $100\,h^{-1}\,\mathrm{Mpc}$) is not insignificant. By using the 'thin-plane approximation,' in which matter in a small redshift interval is projected on to a plane, we are able to show that errors may be introduced. It is not possible to quantify these errors in general, because they will vary from simulation to simulation, depending on the specific mass distributions. However, we show in Section 4.2 that the scaling factors for the computed shear components can vary by as much as 9 per cent through the depth of those simulation boxes contributing the most to the magnification.

The considerations above finally led us to develop an efficient FFT program, whose data output could be manipulated with the appropriate angular diameter distances at every evaluation point. The primary output of the programme is the matrix of second derivatives of the gravitational potential at each of the specified evaluation positions within a periodic three-dimensional distribution of smoothed particle masses.

1.3 Outline of paper

In Section 2 we describe the general principles employed in the standard particle–particle, particle–mesh (P^3M) algorithm, and then how it has been extended for the evaluation of the shear components. We explain the introduction of variable softening into the code, which allows each particle to be represented as a distributed mass. This variable softening smooths away the high-frequency information in very high-density clumps, thus avoiding strong scattering, and also allows particles in low-density regions to be spread more widely to give more realistic density values.

In Section 3 we describe our testing procedures for the code. The first of these compares the computed shear components at a large number of points surrounding a single massive particle, with values derived from the Ewald (1921) summation technique. The second test compares values of the normalized trace of the shear matrix with density values derived using an independent method, a smoothed particle hydrodynamics (SPH) algorithm.

Section 4 emphasizes two advantages of our new algorithm. First, we demonstrate the slow convergence of shear values to their true values, as increasingly large volumes of matter are included surrounding an evaluation position. This suggests the need, in general, to include the effects of matter well beyond a single period transverse to the line of sight. Secondly, we show that, by considering all the matter in a cubic simulation to be at the same angular diameter distance, sizeable errors may be introduced to the absolute shear values, and to calculations of the magnification along a line of sight.

Section 5 describes the cosmological *N*-body simulations we are using for the application of the new algorithm, and explains our choice of the appropriate minimum value for the variable softening. The multiple lens-plane theory (described by Schneider, Ehlers & Falco 1992) is summarized for the determination of magnification distributions along large numbers of lines of sight through the simulations. We then provide some preliminary results to show the efficacy of the method. These include (a) plots of the magnification as it develops along a line of sight, (b) values for the shear and convergence in a given cosmological simulation, and (c) distributions of the magnification due to weak lensing for isolated simulation boxes. Finally, we outline our proposed future work, which will link simulations together to provide a complete realization from a distant source to an observer in the present epoch. This will enable us to compare the results from different cosmologies.

Section 6 summarizes our conclusions about the algorithm and its applicability.

In Appendix A we describe how the peculiar potential relates to that in a universe with large-scale homogeneity. We show how use of the peculiar potential, which takes account of departures from homogeneity through the subtraction of a term including the mean density, allows the shear to be correctly computed.

In Appendix B we investigate rigorously the equivalence between two-dimensional and three-dimensional periodic approaches, in the absence of discrete angular diameter distances within the realizations. The treatment details the conditions under which the two approaches may be considered to be equivalent.

In Appendix C we summarize the Ewald (1921) summation method, which we have used to assess the accuracy of our new code. We describe the method in outline, and compare the treatment with the P^3M method. Finally, we develop the equations for the summation method which we have used in the testing of the results from our new algorithm.

2 IMPLEMENTATION

In this section we describe the numerical method used for measuring the local three-dimensional shear in simulation data. The technique is an extension of the standard P^3M algorithm familiar from cosmological particle codes. We begin with a brief review of the P^3M method, and then describe how it has been extended for the shear calculation.

2.1 The P^3M algorithm

The P^3M algorithm was developed in the context of particle

simulations of plasmas by Hockney, Eastwood and co-workers (see Hockney & Eastwood 1988 for a full description) as an efficient method for calculating the pairwise interactions of a large number of particles. In the cosmological context, with the method being used to calculate forces arising from a large number of self-gravitating particles, the method has two important attractions. First, for a nearly uniform distribution of particles, the computational cost is of order $N \log_2 N$, where N is the number of particles, rather than the normal $O(N^2)$ scaling behaviour expected for a naıve computation of the forces on N particles from each of their $(N-1)$ neighbours. The second attractive feature for cosmology is that the method, in its standard form, has periodic boundary conditions, and thus lends itself naturally to the simulation of a small part of the universe with the remainder being approximated by periodic images of the fundamental volume.

The key idea in the method is to decompose the pairwise interparticle force into a long-range and a short-range component which together sum to the required force. With a suitable choice of the decomposition we can ensure that the short-range force is compact (that is, it is non-zero only within a finite radius, i.e., the 'search radius'), and that the long-range component has a band-limited harmonic content such that it can be accurately represented by sampling with a regular grid of a convenient mesh size. The total force is then accumulated on particles by summing directly a contribution corresponding to the short-range component of the force from nearby particles within the search radius, together with the long-range component which is interpolated from a smoothly varying force derived from the regular mesh.

In practice, the calculation of the short-range force [from the direct particle–particle (PP) sum over near neighbours] and the long-range force [from the particle–mesh (PM) field calculation] depend on each other only to the extent that the accumulated force from the two should sum to the required total force. The two calculations may be performed in either order: here we shall describe the PM calculation first.

The heart of the PM calculation is the solution of Poisson's equation on a grid via a rapid elliptic solver; the method used here is FFT convolution. A mesh-sampled density is obtained by smoothing the particle distribution on to a regular grid with an appropriate kernel. The properties of the kernel are chosen to filter the high frequencies present in the distribution so that the smoothed distribution may be adequately sampled by the mesh. The mesh potential is then obtained from the mesh density by FFT convolution. An advantage of using an FFT method is that it is possible to substantially reduce translational and directional errors in the mesh-computed quantities by judicious adjustment of the Fourier components of the Green's function. For the standard force calculation, the components of the Green's function are optimized such that the rms deviation of the computed force from the desired force is minimized. Full details of these techniques may be found in Hockney & Eastwood (1988). A key feature of the method is that the Fourier-transformed density field may be smoothed by using a high-frequency filter. This suppresses aliasing and leads to a more accurate pairwise force; that is, one which has less positional and rotational dependence relative to the grid.

Derivatives of the potential may then be obtained at mesh-points using standard finite-difference techniques. A 10-point differencing operator is used here to minimize directional errors in the computed differences (see Couchman, Thomas & Pearce 1995). Values of the potential and its derivatives at arbitrary points in the computational domain are then obtained by interpolation from the mesh values. (Using the same kernel for interpolation as was used for particle smoothing ensures that particles do not experience self-forces in the standard P^{3}M method.)

The accumulation of the PP component of the force on a particle from near neighbours is achieved by regridding the particles on to a mesh which has a cell size such that the side is equal to the radial distance at which the short-range force falls to zero. This mechanism enables the neighbours contributing to the short-range force to be found efficiently by searching over the cell in which the particle in question lies and its 26 neighbouring cells. A disadvantage of this technique is that as particle clustering develops in a simulation the average number of neighbours rises, causing the method to slow as the number of PP contributions which must be computed increases. A technique to overcome this deficiency in simulation codes has been developed (Couchman 1991), but the problem will not be of concern in this paper where we shall be concerned only with limited clustering.

The method leads to accurate interparticle forces with the force error (arising from the mesh aliasing) being controlled by the degree of high-frequency filtering employed in the Fourier convolution. A greater degree of attenuation of the high-frequency components reduces the error but leads to a 'smoother' mesh force. This requires that the direct-sum search be performed out to larger radii, which in turn requires a search over a greater number of particles, leading to a slow-down in the execution of the code.

The method may be described schematically in the following terms. Suppose that the total pairwise potential required is $\varphi = \varphi(r)$, where r is the radial distance from a particle. Then we compute this as $\varphi = \varphi_{\rm PP} + \varphi_{\rm PM}$, where $\varphi_{\rm PP}(r) = 0$ for $r > r_{\rm c}$ is the PP component, and $\varphi_{\rm PM}$ is the mesh part. The functional form of φ is Coulombic on large scales (neglecting for the moment the effect of the periodic images), with perhaps a softening at small scales to allow for the fact that each particle may represent a very large astrophysical mass, and to ameliorate certain numerical problems in the simulation code such as two-body scattering.

2.2 Adaptation of the P^{3}M algorithm for the calculation of the shear components

The P^{3}M method computes forces, or first derivatives of the potential, ϕ, at a point by splitting the contribution of the density distribution into two components as described above. The potential itself is also computed as a simulation diagnostic in many standard P^{3}M implementations using the same splitting technique. In principle, any other non-local function computed from the field may be treated in the same way, and this is the approach taken here for the shear components, $\partial^2\phi/\partial x_i \partial x_j$. The implementation details specific to the calculation of the shear values will be discussed here.

The short-range part of the shear field at a point is accumulated directly from neighbouring particles from the appropriate Cartesian projections of the analytic function:

$$\left(\frac{\partial^2 \phi}{\partial x_i \partial x_j}\right)_{\rm PP} = \sum \frac{\varphi'_{\rm PP}}{x}\,\delta_{ij} + \left(\varphi''_{\rm PP} - \frac{\varphi'_{\rm PP}}{x}\right)\frac{x_i x_j}{x^2}, \qquad (1)$$

where the sum is over all neighbour particles, and x is the separation of a neighbour particle from the point at which the shear is desired. (We have used the prime notation to denote

derivatives with respect to radial separation.) The short-range part of the field may be computed to machine accuracy.

The long-range part of the shear field is derived by taking a second difference of the force values as computed in the standard P^3M method. The only difficulty is that differencing the mesh field magnifies the noise which is present as a result of aliasing. Reducing this noise requires more filtering in the Fourier domain, with a corresponding increase in the short-range cut-off, r_c.

Optimization of the Green's function appropriate for the shear calculation is done in a manner similar to that used for the force calculation. We minimized the sum of the squares of the deviations of all nine components of the shear, although a number of other reasonable possibilities exist. Minimizing the deviation of the diagonal components, for example, produced results that were little different.

It would be possible to compute the mesh shear components by inverse Fourier transform of $-k_i k_j \tilde{\phi}(\boldsymbol{k})$ directly for each i, j such that $1 \leq i \leq j \leq 3$, thus avoiding the real-space differencing. It would still be necessary to filter the field, however, and for the differencing operator used, the very small increase in accuracy would not justify the added computational cost of several further FFTs.

2.3 Particle softening

An important feature of numerical particle codes is the use of particle 'softening'. The effect of this is that each particle in the code represents not a point mass but a distributed mass with some given (fixed) radial profile. Softening is introduced primarily to avoid artificial (or numerical) relaxation, i.e., close two-body encounters leading to spurious energy redistribution in the system. Since in most simulations we are attempting to model the cosmic matter density as a collisionless fluid, this is a useful approach. (Note that the particle softening referred to here is distinct from the high-frequency filtering, or smoothing, employed in the PM part of the calculation.)

In numerical particle simulation codes it is usual to employ a global softening for all particles (which may, however, vary in time). As the particle distribution evolves and particles cluster the low-density regions are represented by fewer particles. In a simulation computing interparticle forces to evolve the distribution of particles, this is of little consequence. However, if we wish to compute the shear values at some position on a ray passing through a low-density region it may never come within the softening of the widely spread particles in the region. Since we are interested in the trace of the shear matrix, which is equivalent to the density, this would suggest that the density at this point was zero. (In fact, the density would be negative, since the total mass in the periodic simulation cube must be zero.) This is unrealistic and does not accurately represent the matter density in these regions. Increasing the softening would ameliorate this situation in the voids, but would smooth away the high-frequency information present in regions where the particles have clustered into high-density lumps.

The approach we have taken is to employ a variable softening, such that a particle in a region of low particle density has a 'size' which is greater than that of a particle in a high-density region. We have chosen a criterion similar to that used in hydrodynamic simulations using the SPH method (e.g. Gingold & Monaghan 1977). Each particle is chosen to have a softening such that its sphere of influence is proportional to the distance to its 32nd nearest neighbour. Given these values, the code appropriately modifies the short-range (PP) calculation to increment the shear components at a given point, taking into account the varying sizes of the neighbouring particles.

3 PERFORMANCE AND TECHNICAL ASSESSMENT

3.1 Pairwise shear tests

A minimal check of the technique may be made by computing the shear components at a large number of points surrounding a single massive particle. This is a useful test, because the result is known analytically and it provides an immediate assessment of the errors present in the method.

The test was made as follows. A single massive particle was placed at a random location in a mesh cell and the code used to measure the shear components at 16 384 surrounding points located randomly in direction and distributed in radius such that there was an equal number of points per equal logarithmic increment in radius. The test was then repeated a further 34 times, using the same evaluation positions but different locations for the test particle designed to sample adequately the mesh cell. The shear components measured at each location were then compared with the true values derived from the Ewald (1921) summation technique as described in Appendix C. These comparisons are plotted in Fig. 1.

Panel (a) of Fig. 1 shows the absolute value of the radial component of the shear (solid line) as well as the fractional error in this quantity (scattered dots). Panel (b) shows the same quantities for the two transverse components. In both cases the measured values have been multiplied by an appropriate power of the separation, r, such that a pure Coulombic potential would show no radial variation. For the filtering chosen, the maximum error in these quantities is approximately 7 per cent, and occurs near the mesh smoothing used. The values of the radial and transverse components have been plotted as a series of dots, one for each test separation, which merge into a solid line. The line thickening around a separation of 0.05 reflects larger errors in these quantities. At separations beyond about 0.3, the spread in the values reflects the true anisotropy of the shear components. (Note that the fractional errors remain small unless the quantity itself becomes small.)

The test was performed using a mesh of 64^3 cells, but the errors are essentially independent of the mesh size for typical values of the softening. The leftmost dotted vertical line marks the size of the mesh cell. The second dashed vertical line marks the size of the neighbour search cell in the direct accumulation of the shear components. The smoothness of the mesh-computed components allows the search radius to be slightly smaller than twice the softening (the radius at which the force would become Coulombic), with an error no greater than that arising from the mesh calculation. The resulting small discontinuity is just visible in the radial component of shear in panel (a), and in panels (c) and (d). The cyclic error at small separations arises because linear interpolation into a look-up table is used for the short-range force. The few points lying above the main scatter of errors in panel (b) are due to one of the transverse components becoming very small, with the consequence that the fractional error can become large. The rms error in our test on a single particle is less than 2 per cent.

Panel (c) plots the absolute value of the trace of the Ewald-computed shear matrix and the fractional error of the computed

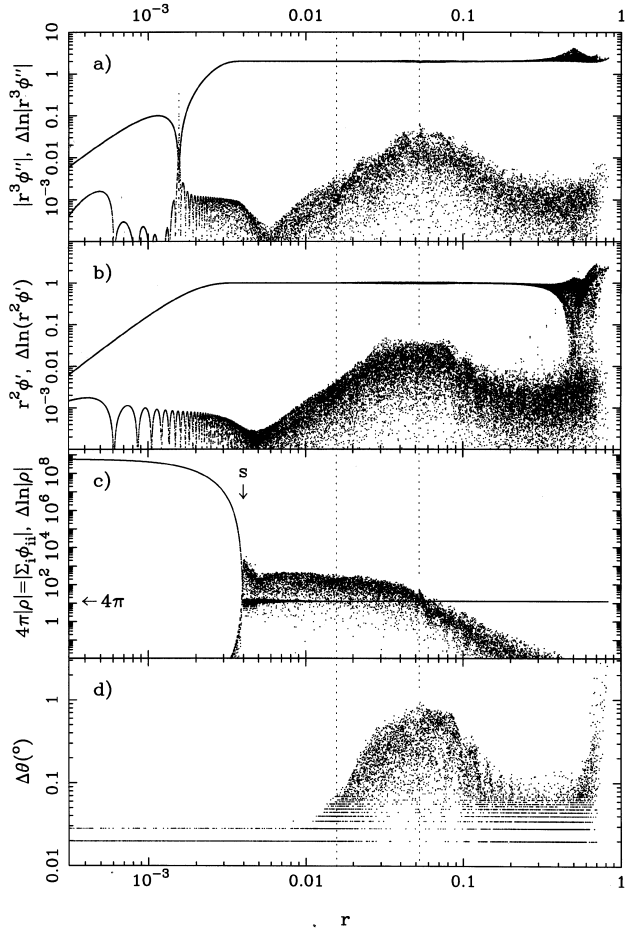

Figure 1. Computed shear components and errors in these components arising from the single-particle test described in Section 3.1. The solid lines in panels (a) and (b) show the radial and transverse components of the shear respectively, normalized so that values arising from a Coulombic potential would be constant. The scattered dots show the fractional error in these quantities. Panel (c) shows (solid line) the absolute value of the trace of the shear values (4π times the density) and the fractional error in that quantity. The panel shows the value of the effective particle softening used, indicated by *s*, and the absolute value of the trace expected in the empty background in a periodic system ($|-4\pi|$) beyond the softening. Panel (d) shows the directional error in the principal eigenvalue of the shear matrix in degrees. The two vertical lines show the cell size (1/64) and the search cell radius (here 3.37/64). For a complete description of the test and of the features shown in the figure, refer to the text. All separations, *r*, are expressed in units of the system's period.

trace values. The particle softening chosen for this test was 0.002 in units of the box side dimension and, because of the definition of the particle softening employed, this corresponds to the particle having a radial extent of 0.004. The true value of the trace for smaller separations thus reflects 4π times the density of the particle as required by Poisson's equation. At larger separations the true density is -1 (since the total mass in the system has to be zero), and thus the Ewald-computed shear is 4π. Large errors occur in the trace values, simply because the shear values individually are many orders of magnitude larger than 4π and each is in error by a few per cent; we thus cannot expect the sum of these large values to cancel to high precision to give the required result. This fact was one of the primary motivations for using a variable softening in which every position at which the shear was measured would lie within the effective radius of some particle. In this case we may expect that the computed values of the trace will have roughly the same fractional error as shown in panels (a) and (b). This is discussed and tested further in the next section.

Finally, panel (d) shows the directional error between the principal eigenvector of the computed shear matrix and the separation vector. (The banding for small directional errors is due to numerical quantization in the computation of the directional error.) It is apparent that directional errors are very small in this method.

Note that the errors in the shear values computed from an *ensemble* of particles are, in general, much smaller than the pair-wise errors shown in Fig. 1. (For ensembles used in typical *N*-body simulations, the rms force errors are typically 0.3 per cent.) This is because the Fourier representation of a general particle distribution will have a smaller high-frequency content than the equivalent representation of a single massive particle, and can thus be represented better by a given fixed grid. Only if the PP and PM forces almost exactly cancel will the *fractional* errors be larger, although in this case the absolute error will be small. There will be no appreciable change in the error values with larger mesh configurations normally used with *N*-body simulation data.

3.2 Comparison of measured trace and overdensity for a distribution of particles

For a more realistic test of the code, we compare the computed shear trace with the density evaluated using a standard SPH algorithm for one of our cosmological simulation boxes, described in Section 5.1. The SPH program evaluates a parameter, *l*, at each particle in the simulation box, representing half the distance to the 32nd nearest neighbour. This parameter defines the volume for the density calculation, and the same parameter is applied in the shear code to establish an appropriate value of the softening for the particle. In addition, a specific smoothing function may be used to distribute the mass throughout the volume so defined.

To make a suitable comparison with the shear trace values, we have computed overdensity values from these densities, and compared the ratio of the overdensity and the trace with the overdensity values. In Fig. 2 we plot the average value of this ratio in each overdensity bin. We have used a minimum value of 0.0005 for the variable softening, and analysed the data from 10 000 particle positions.

Because of the very different ways in which the densities are determined (from the shear trace in the new code, and from particle numbers in the SPH program, and the differing shapes of the softening functions used), we expect some dispersion in the values at all densities, and this is indicated by the 1σ error bars. The form of the plot is easily understood throughout its entire range. At low densities, the SPH density values are underestimated, because isolated particles do not have the requisite number of nearest neighbours within the particle mesh. At high densities, the particle softenings will be at the same minimum level for all the particles, retarding the amount of increase in the shear trace values as the real density continues to rise. This effect causes the upturn shown in Fig. 2, which occurs at the overdensity value of 4.5×10^3 for a minimum softening of 0.0005.

The equality of the particle overdensities and shear trace values over more than three decades in density gives us considerable confidence in the use of the shear algorithm generally, and for trace values determined at particle positions, or within the softening range.

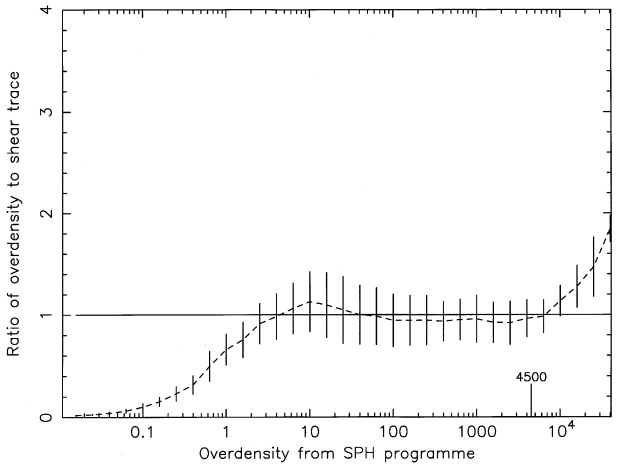

Figure 2. Ratio of overdensity from an SPH program to the normalized shear trace, against the binned overdensity. The average values of the ratio are shown by the broken line; the full line is drawn at the value of unity for comparison. The upturn occurs at the overdensity value of 4.5×10^3, as indicated, for a minimum softening of 0.0005.

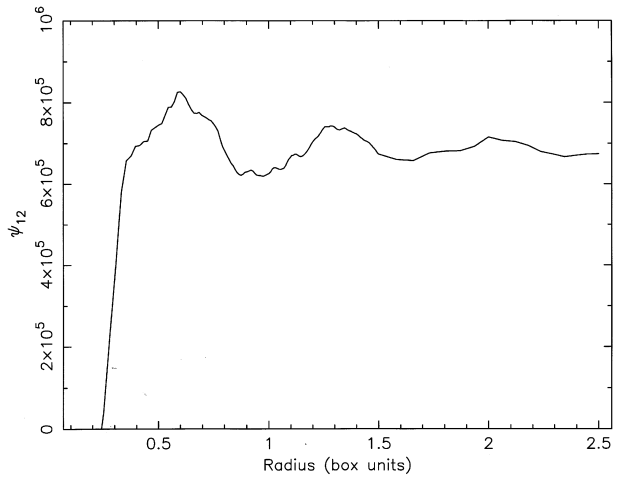

Figure 3. One of the two-dimensional shear components, ψ_{12} ($= \partial^2\phi/\partial x\partial y$), as a function of the radial extent of matter included.

4 SOME ADVANTAGES OF THE THREE-DIMENSIONAL METHOD

4.1 Convergence to limiting values

In the introduction we outlined some of the considerations we made before developing the new three-dimensional algorithm. We expressed concern that shear values in general may converge only slowly to their true limiting values as increasingly large volumes of matter are included around an evaluation position. If so, it would be essential either to take full account of the periodicity of matter orthogonal to the line of sight, or to include the effects of matter over considerable distances from the line of sight.

We investigated this rate of convergence of the shear values for one of our simulation boxes (which we describe in Section 5.1). By using a straightforward direct-summation method for the particle contributions to the shear, we evaluated one of the off-diagonal two-dimensional shear components as we progressively added mass out to a radial extent of 2.5 box units. Beyond a radius of 0.5 from the central position, the particles were laid down with the periodicity of the fundamental volume. The depth was one box unit throughout, because of the inbuilt periodicity along the line of sight. (We show in Appendix B that provided there is periodicity along the line of sight, the two-dimensional shear values will equate with the three-dimensional results integrated over a single period.)

Fig. 3 clearly shows that by including the matter within a single period only (to a radius of 0.5), values for the shear components will, in general, be seriously in error. Of course, different simulations and particle distributions will display different rates of convergence to the limiting values. However, it is quite clear that by making correct use of the periodicity in simulations (as an approximation to the distribution of matter outside of each simulation cube), together with the net zero-mass requirement, more realistic component values are achieved. Other approaches which do not employ these two conditions may suffer from inadequate convergence to the limiting values.

4.2 The effects of angular diameter distances

Our three-dimensional approach allows the use of the appropriate angular diameter distances at every single evaluation position. This is not possible in two-dimensional approaches, where it is assumed that all the lensing mass is projected on to a plane at a single angular diameter distance.

By definition, the angular diameter distance of a source is the distance inferred from its angular size, assuming Euclidean geometry. In an expanding universe, therefore, the angular diameter distance becomes a function of the redshift of the source (and of the observer). In addition, the inclusion of excess matter within the beam causes the beam to become more focused, and makes the source appear closer than it really is. By considering the universe to be populated by randomly distributed matter inhomogeneities, but resembling the Robertson–Walker, Friedmann–Lemaître model on large scales (see Schneider et al. 1992), a second-order differential equation is obtained for the angular diameter distance, D, in terms of the density parameter, Ω, for the universe, and the redshift, z, of the source:

$$(z+1)(\Omega z+1)\frac{\mathrm{d}^2D}{\mathrm{d}z^2}+\left(\frac{7}{2}\Omega z+\frac{\Omega}{2}+3\right)\frac{\mathrm{d}D}{\mathrm{d}z}+\frac{3}{2}\Omega D=0. \qquad (2)$$

Dyer & Roeder (1973) made assumptions about the type of matter distribution to obtain a more general and practical equation. They assumed that a mass fraction, $\bar{\alpha}$ (called the smoothness parameter), of matter in the universe is smoothly distributed, and that the fraction $(1-\bar{\alpha})$ is bound into clumps. Then the equation for the angular diameter distance becomes

$$(z+1)\,(\Omega z+1)\frac{\mathrm{d}^2D}{\mathrm{d}z^2}+\left(\frac{7}{2}\Omega z+\frac{\Omega}{2}+3\right)\frac{\mathrm{d}D}{\mathrm{d}z} + \left[\frac{3}{2}\bar{\alpha}\Omega+\frac{|\sigma|^2}{(1+z)^5}\right]D=0, \qquad (3)$$

in which shear, σ, is introduced by the matter distribution around the beam. They considered the following scenarios for the application of this equation. First, they considered a universe in which all the matter is bound into clumps, so that $\bar{\alpha}=0$, and in which the light beam passes far away from the clumps. This is described as light propagating through an 'empty cone,' and gives rise to maximal divergence of the beam. The second scenario is more general and practical, in that it uses an intermediate value for the smoothness parameter ($0<\bar{\alpha}<1$), but still requires the beam

to pass far away from the clumps. In this case the beam contains a proportion of the smoothed matter distribution which introduces convergence, and hence some degree of focusing. The third scenario has $\bar{\alpha} = 1$, i.e., an entirely smooth universe. Here the smooth matter distribution is present within the beam, giving a 'full-cone,' or 'filled beam' approximation.

In all of these scenarios the term including the shear in equation (3) is minimized, so that the final 'Dyer–Roeder equation' becomes

$$(z+1)(\Omega z+1)\frac{\mathrm{d}^2 D}{\mathrm{d}z^2}+\left(\frac{7}{2}\Omega z+\frac{\Omega}{2}+3\right)\frac{\mathrm{d}D}{\mathrm{d}z}+\frac{3}{2}\bar{\alpha}\Omega D=0, \quad (4)$$

and can be solved for different values of Ω and $\bar{\alpha}$. For $\Omega = 1$ and $\bar{\alpha} = 1$ (filled beam), Schneider et al. (1992) quote the result for the angular diameter distance between an observer at redshift z_1, and a source at redshift z_2, as

$$D(z_1, z_2) = \frac{c}{H_0} 2\left[\frac{1}{(1+z_1)^{\frac{1}{2}}(1+z_2)} - \frac{1}{(1+z_2)^{\frac{3}{2}}}\right], \quad (5)$$

or

$$D(z_1, z_2) = \frac{c}{H_0} r(z_1, z_2), \quad (6)$$

where $r(z_1, z_2)$ is the dimensionless angular diameter distance, c is the velocity of light, and H_0 is the Hubble parameter.

Magnification values, μ, derived using Dyer & Roeder's angular diameter distances will be affected according to the approximation used. For example, rays passing close to clumps or through high-density regions will result in magnification in any approximation. If the empty-cone approximation is used, then μ will be greater than 1, and if the full-cone approximation is used, then μ will be greater than the mean magnification, $\langle\mu\rangle$, which is also unity. Rays passing through voids will have $\mu = \mu_{\min} = 1$ in the empty-cone approximation (since the rays will be far from all concentrations of matter, and will satisfy the empty cone conditions). In the full-cone approximation, $\mu < 1$ because the rays will suffer divergence. However, the minimum value in this case will be (Schneider et al. 1992)

$$\mu_{\min} = \left[\frac{D(z; \bar{\alpha} = 1)}{D(z; \bar{\alpha} = 0)}\right]^2. \quad (7)$$

In the testing of our new algorithm we have used the filled-beam approximation ($\bar{\alpha} = 1$) to obtain the angular diameter distances. With variable softening, most of the rays will pass through a slowly varying density field, justifying this choice, although the smoothness parameter should be different from unity, and possibly should evolve slowly with time. (Tomita 1998b finds, by solving the null-geodesic equations for a large number of pairs of light rays in four different cosmological N-body simulations, that the best value for $\bar{\alpha}$ is almost equal to 1, though with considerable dispersion.) However, the approximation that all rays should pass far from the clumps will not be strictly true, as shear on the light rays will be very much in evidence.

We show in Fig. 4 the value of the factor $r_{\rm d}r_{\rm ds}/r_{\rm s}$, where $r_{\rm d}$ is the dimensionless angular diameter distance from the observer to the lens (here, the front face of each simulation box), $r_{\rm ds}$ is that between the lens and the source, and $r_{\rm s}$ is that for the observer–source. We have taken the sources to be at redshifts of 5, 4, 3, 2 and 1. This factor, $r_{\rm d}r_{\rm ds}/r_{\rm s}$, is used to multiply the shear component values generated in the code, and we see that it has a peak near $z = 0.5$ for a source redshift of 5. The curves are very steep near

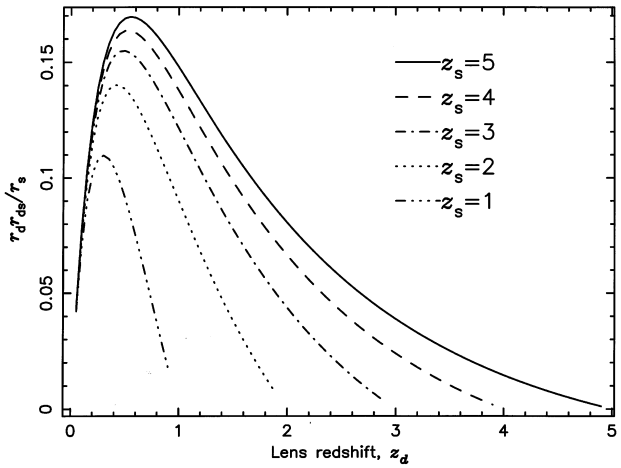

Figure 4. The factor $r_{\rm d}r_{\rm ds}/r_{\rm s}$ as functions of the lens redshift, $z_{\rm s}$, assuming sources at redshifts of 5, 4, 3, 2 and 1.

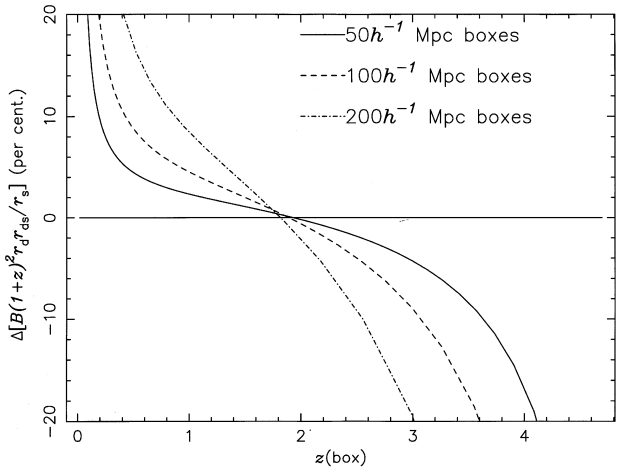

Figure 5. The percentage difference in the multiplying factor for the shear component values generated by the code, between the front and back faces of each simulation box. The figure shows the differences for simulation boxes of different comoving depths, highlighting possible errors associated with plane projections. For the boxes near to a redshift of 0.5, the box depths in redshift space are approximately 0.03 for $50\,h^{-1}$ Mpc boxes, 0.06 for $100\,h^{-1}$ Mpc boxes, and 0.12 for $200\,h^{-1}$ Mpc boxes.

$z = 0$, indicating large fractional differences between the values of $r_{\rm d}r_{\rm ds}/r_{\rm s}$ at the front and the back of each simulation box at late times, where considerable structure may also be present.

We show later, in equation (10), Section 5.3, that the two-dimensional 'effective lensing potentials' are obtained from the three-dimensional second derivatives of the gravitational potential. To evaluate the absolute effective lensing potentials we must introduce the appropriate scaling factor, which applies to the simulation box dimensions. From equation (10), we can extract the factor $B(1+z)^2 r_{\rm d}r_{\rm ds}/r_{\rm s}$, where $B = (c/H_0)(2/c^2)GM_{\rm part} \times$ (comoving box depth)$^{-2}$. (G is the universal gravitational constant, and $M_{\rm part}$ is the particle mass.) For the simulation boxes we have used, which have comoving dimensions of $100\,h^{-1}$ Mpc, $B = 3.733 \times 10^{-9}$. The $(1+z)^2$ factor occurs to convert the comoving code units into physical units. By evaluating the factor $B(1+z)^2 r_{\rm d}r_{\rm ds}/r_{\rm s}$ at the front and rear faces of each simulation box, we can obtain an estimate of the maximum error associated with projecting the mass distribution on to a plane. In Fig. 5, we plot the percentage differences in this factor between the front and

rear faces of each simulation box, and show the results for boxes of 50, 100, and $200\,h^{-1}$ Mpc comoving depths. The figure clearly indicates the possible presence of large errors when boxes are treated as plane projections. The errors are considerable at high and low redshifts, and, in particular, they are significant near $z = 0.5$, where the angular diameter factor $r_{\rm d}r_{\rm ds}/r_{\rm s}$ is greatest. For simulation boxes of $50\,h^{-1}$ Mpc the difference is 4.5 per cent near $z = 0.5$, for boxes of $100\,h^{-1}$ Mpc the difference is 9.0 per cent, and for boxes of $200\,h^{-1}$ Mpc the difference is 16.3 per cent, for a source at $z = 5$. These differences in the multiplying factors are, of course, the maximum differences, and would apply to the contribution to the shear from particles located in the far face of the simulation box if the mass distribution were projected into the near face. Consequently, the actual error in the two-dimensional shear values computed from all the particles depends entirely on the specific distribution of particles, and in general will be lower than the figures indicated in Fig. 5. The actual errors introduced may also be reduced if the projection is made on to a plane midway through the simulation box depth, although, again, the error value will depend on the specific particle distribution.

Obviously, the front–rear differences are smallest in the smallest boxes (here $50\,h^{-1}$ Mpc comoving depth), but with small simulation boxes there are problems in adequately representing the extent of large-scale structure, and, as we have seen in Section 4.1, a serious question as to whether two-dimensional shear values can be correctly determined by considering matter out to such small radii in the transverse direction. Even with $100\,h^{-1}$ Mpc boxes we have shown that the two-dimensional shear values can be seriously in error when only matter within the fundamental volume is included. With $200\,h^{-1}$ Mpc boxes, better convergence of values may be obtained because of the larger spread of matter transverse to the line of sight; however, the range in the angular diameter distance factors along the line of sight is greater, introducing larger errors. To reduce this error, it may be thought that the boxes could be divided into a number of planes; however, this procedure would give erroneous values for the shear because a full single period in depth is required, as we show in Appendix B.

In Section 5.3 we show that an approximation for the magnification in weak lensing is

$$\mu \simeq 1 + (\psi_{11} + \psi_{22}), \tag{8}$$

where the ψ values are the two-dimensional 'effective lensing potentials,' derived from integrating the three-dimensional components. Consequently, we may also find that the errors in the shear component values, arising from ignoring the angular diameter distance factors through the simulation boxes, enter into calculations of the magnification.

5 APPLICATION OF THE CODE TO LARGE-SCALE STRUCTURE SIMULATIONS

5.1 Brief description of the LSS simulations used

Our three-dimensional shear code can be applied to any three-dimensional distribution of point masses confined within a cubic volume. Each particle may be assigned an individual mass, although in our tests of the code we have assumed all the particles to have the same mass. In addition, the code allows for either a fixed softening value for each particle, or a variable softening, dependent on each particle's density environment.

We applied the code to the data bank of cosmological *N*-body simulations provided by the Hydra Consortium (http://www.astro.uwo.ca/hydra_consort/data/data.html) and produced using the 'Hydra' *N*-body hydrodynamics code (Couchman et al. 1995).

Our initial tests, described here, have used individual time-slices from these simulations using 128^3 particles with a cold dark matter (CDM) spectrum in an Einstein–de Sitter universe. Each time-slice has comoving sides of $100\,h^{-1}$ Mpc. Since each is generated using the same initial conditions, we arbitrarily translate, rotate and reflect each time-slice to prevent the formation of unrealistic correlations of structure along the line of sight, when the boxes are linked together. The simulations used have density parameter $\Omega_0 = 1$ and cosmological constant $\Lambda_0 = 0$. The power spectrum shape parameter, Γ, has been set to 0.25, as determined empirically on cluster scales (Peacock & Dodds 1994), and the normalization, σ_8, has been taken as 0.64 to reproduce the number density of clusters (Vianna & Liddle 1996). The dark matter particle masses are all $1.29 \times 10^{11}\,h^{-1}$ solar masses.

5.2 The choice of softening

We have chosen a softening function for the radial distribution of mass for each particle, such that light rays feel the existence of a smooth mass distribution. Our code also allows for variable softening, so that each particle may be assigned its own softening-scale parameter, depending on the particle number-density in its environment. In this way, it can be used to minimize the effects of isolated single particles, whilst the smoothed denser regions are able to represent the form of the large-scale structure. The parameter we have chosen to delineate the softening scale for each particle is proportional to l, where $2l$ is the radial distance to the particle's 32nd nearest neighbour. The value of l is evaluated for every particle by applying our SPH density program, as described in Section 3.2, to each simulation box.

We allow the maximum softening to be of the order of the mesh dimension for isolated particles, which is defined by the regular grid laid down to decompose the short- and long-range force calculations. In this way the density values are improved, as we described in Section 2.3. This also means that individual isolated particles are unable to strongly influence the computed shear values, in accordance with our need to study the broad properties of the large-scale structure, rather than the effects of individual particles.

Our new algorithm works with the ratio of the chosen softening (proportional to l) for each particle, to the maximum value (dependent on the mesh size), so that the parameter used has a maximum of unity. Our method, which employs the variable softening facility, contrasts markedly with that of other workers. As an example, Jaroszyński et al. (1990), who evaluate deflections due to density columns projected on to a plane, apply no softening function, except to assume that all the mass within each column is effectively located at its centre.

In the CDM simulations we have used, the minimum values for $2l$ are of order 10^{-3}; e.g., for the redshift $z = 0.4986$ box, the minimum $2l = 1.023\,83 \times 10^{-3}$, (equivalent to $68\,h^{-1}$ kpc). This is comparable to the Einstein radius, $R_{\rm E}$, for a large cluster of 1000 particles (for which $R_{\rm E} = 82\,h^{-1}$ kpc for a lens at $z = 0.5$ and a source at $z = 1$). Consequently, by setting a working minimum value for the variable softening of 10^{-3}, we would rarely expect to see strong lensing due to caustics in our simulations. Also, the

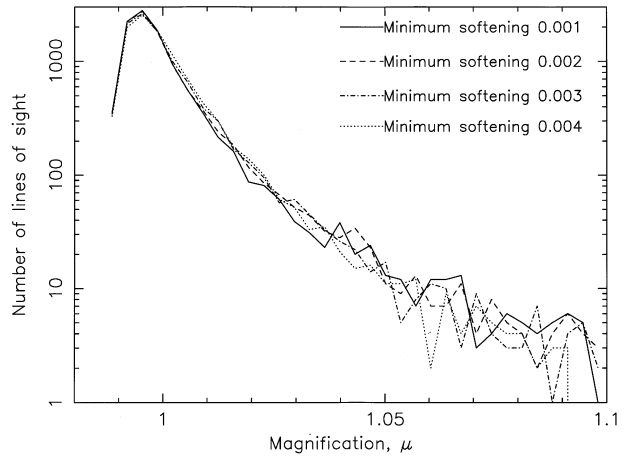

Figure 6. Magnification distributions for various minimum softenings, 0.001, 0.002, 0.003 and 0.004 in box units, for a simulation box at $z = 0.4986$ and a source at $z = 1$. Each bin is of width 0.0034 in magnification.

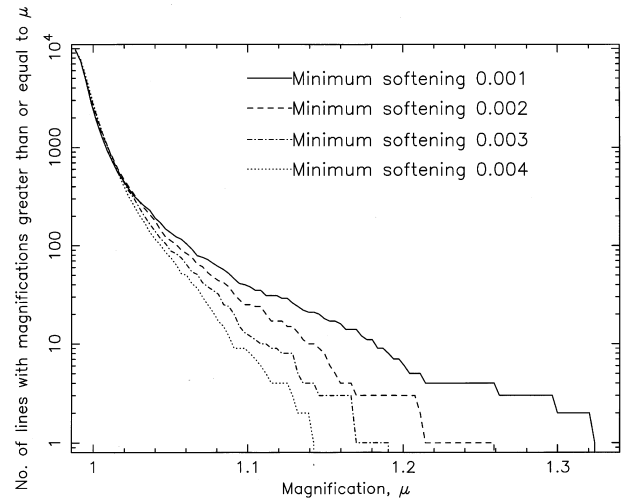

Figure 7. The accumulating number of lines of sight for which the magnification is greater than or equal to μ. The plots show the results of different minimum softenings in a simulation box at $z = 0.4986$, for a source at $z = 1$.

radial extent of this minimum softening is of the order of galactic dimensions, thereby providing a realistic interpretation to the softening.

Having justified our chosen value for a working minimum value, it is also important to understand the sensitivity of our results to the input softening. Fig. 6 shows the distribution of magnifications due to a single (assumed isolated) simulation box ($z = 0.4986$), and a source redshift of 1, using minimum softenings of 0.001, 0.002, 0.003 and 0.004 in box units. All the distributions are very close for 90 per cent of the lines of sight, and show only gradual changes from the lowest to the highest softening values. Only in limited numbers of lines of sight are there significant differences which occur at the high-magnification end.

To highlight the sensitivity to the minimum softening, we plot in Fig. 7 the accumulating number of lines of sight having magnifications greater than or equal to the abscissa value. As expected, we see that the results using the smallest minimum softenings give rise to the highest maximum magnifications.

5.3 Multiple lens-plane theory for magnification distributions

There are two very important properties of our three-dimensional algorithm for shear which make it eminently suitable for use within particle simulations.

First, each simulation box is treated as a periodic system, so that the contributions from all particles and their images are included in the shear computations.

Secondly, as far as we are aware, this is the first algorithm successfully adapted for *N*-body simulations, in which the shear components may be evaluated at a large number of locations throughout the extent of the box. In this way each of the selected locations may be considered as an individual deflection site, and deflections computed using individual angular diameter distances for each site. Two-dimensional planar approaches, by contrast, are able to compute only one deflection for each ray at each projection plane, and such planes will be assumed to be at a single particular angular diameter distance.

The first property of our algorithm gives confidence in the shear component values computed, whilst the second property enables us to trace the behaviour of rays throughout the full depth of each simulation box.

To do this, we construct a rectangular grid of directions through each box. Since we are dealing with small deflections, and are interested only in the statistics of the output values, we consider each light ray to follow one of the lines defined by these directions through the box. The evaluation positions are specified along each of these lines of sight.

The six independent second derivatives of the peculiar gravitational potential are calculated by the code at each of the selected evaluation positions throughout a simulation box. We then integrate the values in small chunks along each line, forming, essentially, a large number of planes through each simulation box. These integrated values form the input data to establish the elements of the Jacobian matrix, $\mathbf{A}$, on each of the lines of sight for each of the deflection sites.

We make use of the multiple lens-plane theory, which has been developed by Blandford & Narayan (1986), Blandford & Kochanek (1987), Kovner (1987) and Schneider & Weiss (1988a, b), and described in detail in Schneider et al. (1992). At the first deflection site from the source we evaluate the components of the Jacobian matrix,

$$\mathbf{A} = \begin{pmatrix} 1 - \psi_{11} & -\psi_{12} \\ -\psi_{21} & 1 - \psi_{22} \end{pmatrix}, \tag{9}$$

in which the two-dimensional 'effective lensing potentials' are obtained from the three-dimensional second derivatives of the gravitational potential:

$$\psi_{ij} = \frac{D_{\rm d} D_{\rm ds}}{D_{\rm s}} \times \frac{2}{c^2} \int \frac{\partial^2 \phi(z)}{\partial x_i \partial x_j} {\rm d}z, \tag{10}$$

where $D_{\rm d}$, $D_{\rm ds}$ and $D_{\rm s}$ are the angular diameter distances from the observer to the lens, the lens to the source, and the observer to the source respectively. At subsequent deflection sites we obtain the developing Jacobian matrix recursively, since the final Jacobian for N deflections is

$$\mathbf{A}_{\rm total} = \mathbf{I} - \sum_{i=1}^{N} \mathbf{U}^i \mathbf{A}_i, \tag{11}$$

where $\mathbf{I}$ is the unit matrix,

$$\mathbf{U}^i = \begin{pmatrix} \psi^i_{11} & \psi^i_{12} \\ \psi^i_{21} & \psi^i_{22} \end{pmatrix} \tag{12}$$

for the ith deflection, and each of the intermediate Jacobian matrices can be written as

$$\mathbf{A}_j = \mathbf{I} - \sum_{i=1}^{j-1} \beta_{ij} \mathbf{U}_i \mathbf{A}_i, \tag{13}$$

where

$$\beta_{ij} = \frac{D_{\rm s}}{D_{is}} \frac{D_{ij}}{D_j}, \tag{14}$$

in which D_j, D_{is} and D_{ij} are the angular diameter distances to the jth lens, that between the ith lens and the source, and that between the ith and jth lenses respectively.

The magnification is, in general,

$$\mu = (\det \mathbf{A})^{-1}, \tag{15}$$

so that we can assess the magnification as it develops along a line of sight, finally computing the emergent magnification after passage through an entire box or set of boxes. For example, Fig. 8 shows the development of the magnification through a single isolated simulation box ($z = 0.4986$) with a chosen source redshift of 1. The slightly different emerging magnifications arise because of the choice of different input minimum softening values. The figure shows an arbitrary line of sight, and we have assumed that the redshift varies linearly through the box. The redshift at the far face of the chosen box, 0.5615, is also the redshift of the first evaluation location for the shear, so that, in general, the first value of the magnification may be different from unity. Where significant shear component values exist, they will be dependent on the set minimum softening value; in Fig. 8 we see that the magnification curves diverge or converge at such locations. At most locations where the shear component values are small, the curves for different softenings are closely parallel, because of the insensitivity to the softening. This feature is also seen in Fig. 8.

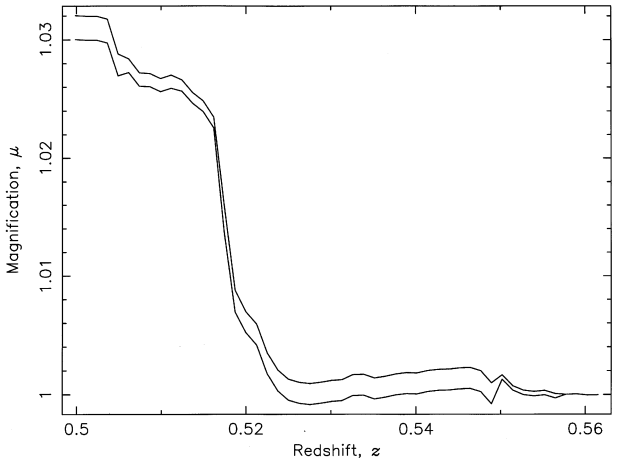

Figure 8. Magnification versus redshift along an arbitrary line of sight, using two different minimum softening values. The lower curve has a minimum softening of 0.001, and the upper curve has a minimum softening of 0.004. The result has been established using a single (assumed isolated) simulation box ($z = 0.4986$) and a source redshift of 1. The redshift has been assumed to vary linearly through the box from $z = 0.4986$ at the front face to $z = 0.5615$ at the far face.

The most significant shear component values along the line of sight selected for Fig. 8 occur at the redshift of 0.5162, for which the angular diameter multiplying factor is $r_{\rm d} r_{\rm ds}/r_{\rm s} = 0.0444$ for a source redshift of 1. If a planar approach were taken, and the matter distribution were projected on to a plane at the midway redshift of 0.5301 for this box, then the appropriate angular diameter multiplying factor would be $r_{\rm d} r_{\rm ds}/r_{\rm s} = 0.0433$, introducing an error of 2.5 per cent to the two-dimensional lensing potentials used in the computation of the magnification. This example highlights the fact that errors introduced in two-dimensional approaches, where only a single angular diameter multiplying factor can be used, depend entirely on the specific distribution of matter. It also highlights the importance of using the appropriate angular diameter distances throughout the depth of each simulation box, which can only be achieved with a three-dimensional approach.

The convergence, κ, is defined by

$$\kappa = \frac{1}{2}(\psi_{11} + \psi_{22}) \tag{16}$$

from the diagonal elements of the Jacobian matrix, and causes isotropic focusing of light rays, and so isotropic magnification of the source. Thus, with convergence acting alone, the image would be the same shape as, but of larger size than, the source.

The shear, γ, in each line of sight is given by

$$\gamma^2 = \frac{1}{4}(\psi_{11} - \psi_{22})^2 + \frac{1}{4}(\psi_{12} + \psi_{21})^2. \tag{17}$$

This is sometimes written in component form:

$$\gamma^2 = \gamma_1^2 + \gamma_2^2, \tag{18}$$

where

$$\gamma_1 = \frac{1}{2}(\psi_{11} - \psi_{22}), \tag{19}$$

and

$$\gamma_2 = \frac{1}{2}(\psi_{12} + \psi_{21}). \tag{20}$$

Shear introduces anisotropy, causing the image to be a different shape, in general, from the source.

With weak lensing, and these definitions, the magnification reduces to

$$\mu \simeq 1 + (\psi_{11} + \psi_{22}) = 1 + 2\kappa. \tag{21}$$

In the presence of convergence and shear, a circular source becomes elliptical in shape, with major and minor axes

$$a = \frac{1}{(1 - \kappa - \gamma)}, \tag{22}$$

and

$$b = \frac{1}{(1 - \kappa + \gamma)}, \tag{23}$$

so that the ellipticity, ϵ, is given by

$$\epsilon = 1 - \frac{b}{a} = 1 - \frac{1 - \kappa - \gamma}{1 - \kappa + \gamma}, \tag{24}$$

which reduces to

$$\epsilon \simeq 2\gamma \tag{25}$$

in weak lensing.

Distributions and relationships amongst all these quantities can be determined straightforwardly. As an example, Fig. 9 shows the shear, γ, and convergence, κ, in a single (assumed isolated) simulation box, ($z = 0.4986$), with a source at redshift $z_s = 1$. The minimum (variable) softening has been set in this case at 0.001. The considerable scatter in the data-points arises because of the expected strong fluctuations in the shear for light rays passing through regions of high density (high convergence). In addition, the shear appears to increase broadly with increasing convergence, as might be expected. Plots of the shear versus the convergence using different values of the minimum softening show similar features. Measurements of the magnification and ellipticity show the linear dependences on κ and γ according to equations (21) and (25), as expected. Small departures from linearity are apparent only at high values of κ and γ.

Fig. 10 is an example of the magnification distributions in three different simulation boxes, which are assumed to be isolated in space. We show the distributions for the $z = 0$ box (which we take to extend from $z = 0$ to 0.0339), the $z = 0.4986$ box ($z = 0.4986$ to 0.5615), and the $z = 1.0404$ box ($z = 1.0404$ to 1.1400), each with minimum softenings of 0.001. (The box labelling follows from the nominal redshifts for the boxes in the original particle simulations.) A source redshift of $z_s = 2$ has been chosen. (All the distributions have a mean magnification value of 1.)

In Fig. 11 we show the results from the same three simulation boxes, for a source at $z = 2$, but here assumed to be all located at the same position ($z = 1.0404$). This allows direct comparisons between the boxes to be made in terms of the formation of structure within them. For example, the later boxes show higher values for the maximum magnifications, and have shallower slopes in the distributions at the high-magnification end. The peaks in the distributions for the later boxes occur at slightly lower magnification values, whilst all have mean magnifications of unity, as required.

By a simple extension of the multiple lens-plane theory, we are now able to take the emergent ψ values from each simulation box, and feed them into a string of subsequent boxes. In this way we are able to obtain all the necessary emergent parameters at $z = 0$ arising from a source at high redshift. We shall be reporting on these results in a future publication.

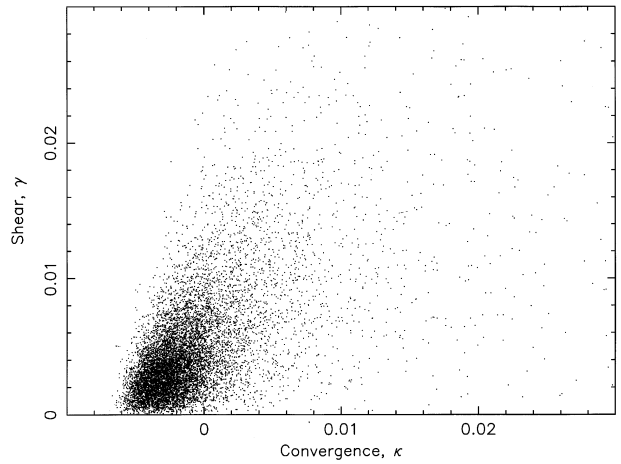

Figure 9. Shear values versus the convergence in a single simulation box ($z = 0.4986$), assumed isolated, with a source redshift of 1. The minimum softening applied is 0.001 in box units. The data points result from evaluating the shear and convergence along 10 000 lines of sight.

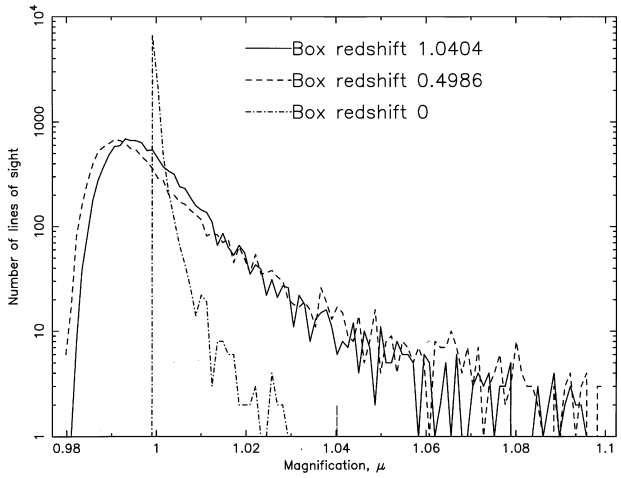

Figure 10. A comparison of the magnification distributions for three different simulation boxes, placed at their correct distances, with a source at $z_s = 2$. The bin widths are 0.0012 in magnification.

6 SUMMARY AND CONCLUSIONS

In this paper we have discussed our motivations for developing a new algorithm for use with cosmological *N*-body simulations in the study of weak gravitational lensing. We have also described the algorithm we have developed together with its variable softening refinement, and we have tested the output results from three-dimensional simulations against the Ewald (1921) summation method for the shear components. We have described how the results from the new code can be applied to realistic simulations by including the appropriate angular diameter distances at every evaluation position. In this way it is very straightforward to compute the final magnifications, source ellipticities, shear and convergence values as a result of the passage of light through linked simulation boxes. The main points we have discussed are the following.

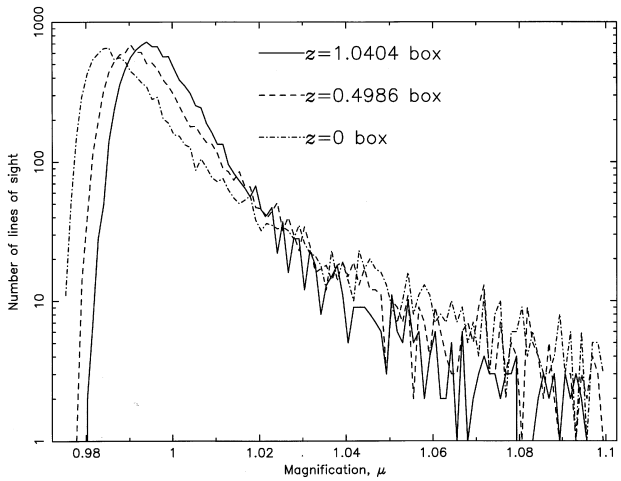

Figure 11. A comparison of the magnification distributions in three different simulation boxes, all assumed to be located at the same redshift, 1.0404. The bin widths are 0.0013 in magnification. The distribution curve for the $z = 1.0404$ box (which is placed at its correct position) is the same as that shown in Fig. 10; small differences occur because of the different magnification bin widths.

(1) Appendix B rigorously shows that results from the two-dimensional and three-dimensional approaches to weak lensing are equivalent only if the mass distribution is periodic along the line of sight, a full period (in depth) is considered, and the angular diameter distances are assumed constant throughout the depth.

(2) In order to evaluate the shear components correctly, it is necessary to work with the peculiar potential, which we describe in Appendix A. This applies equally to two-dimensional and three-dimensional methods.

(3) The results for two-dimensional planar projections may be invalid if matter outside the single period plane (in directions orthogonal to the line of sight) is not included. Because of the slow convergence of the potential and shear components to their limiting values, it is necessary, in general, to include the effects of matter well beyond a single period, but depending on the specific mass distribution.

(4) The inclusion of the appropriate angular diameter distances at every evaluation position within a three-dimensional realization avoids errors in the shear and magnification values. The errors incurred by treating simulation boxes as planes can be a maximum of 9 per cent in a single box of depth $100\,h^{-1}$ Mpc at a redshift of 0.5 (where the lensing effects are greatest for a source at $z = 5$). (At low and high redshifts the maximum fractional errors may be greater.) The maximum errors apply when the plane projection is made on to the 'front face' of the simulation box, but they are dependent on the specific particle distribution within the box.

(5) The output from our algorithm is the three-dimensional shear components evaluated at a large number of positions within a periodic N-body simulation cube. The code itself is a development of the standard P^3M algorithm which determines forces (the first derivatives of the potential) and the potential itself. The short-range part of the shear field at a point is accumulated directly from neighbouring particles, whilst the long-range part is obtained by taking a second difference of the force values. The computational cost of the P^3M method is low, being of order $N \log_2 N$ rather than of order N^2.

(6) The PM calculation uses a FFT method in which the density distribution is smoothed, and can be well sampled by the mesh. The mesh potential is then obtained by FFT convolution. Errors in the method can be minimized by suitable adjustment of the Fourier components of the Green's function.

(7) A key feature of the new algorithm is the facility to input a variable softening parameter. The feature enables particles in low-density regions to have extended softening, so that nearby evaluation positions register a density rather than a complete absence of matter. By contrast, particles in highly clustered regions are assigned low softening values, and a selected minimum softening value is introduced which limits the possiblility of singular (strong lensing) behaviour. The variable softening feature thus enables a much more realistic depiction of the large-scale structure within a simulation to be made and its weak gravitational lensing effects to be computed. Nevertheless, if strong lensing does occur, it will be evident from the determinant of the Jacobian, which may be evaluated at any point along a line of sight. Ray-tracing procedures, however (see, e.g., Wambsganss et al. 1998), are able to indicate directly the possibility of multiple-imaging, where different rays in the image plane can be traced back to the same pixel in the source plane.

(8) In Appendix C we summarize the Ewald (1921) summation method, and develop the equations for use as a comparison with the values for shear obtained with our new algorithm.

(9) By choosing an appropriate filter, we are able to set limits for the maximum errors in the computed shear values from our code. In the tests, the maximum errors in both the radial and the transverse components of the shear are about 7 per cent for the effects of a single particle, when compared with the values obtained using the Ewald formulae. The rms errors are less than 2 per cent, and errors for ensembles of particles, to which we intend to apply the code, are typically 0.3 per cent (rms). The errors in the trace of the shear matrix can be large, because the trace frequently involves the addition of nearly equal and opposite (but large) values. Individually, however, the errors in each component remain small.

(10) We have tested the data also against the output of a completely different program for the density at particle locations. There is good agreement for the normalized density from this program when measured against the shear trace from our new algorithm.

(11) The output from the code can be used together with the multiple lens-plane theory and appropriate angular diameter distances to obtain values for the magnification, source ellipticity, shear and convergence for a large number of lines of sight as they emerge from a simulation box. We show a typical distribution plot for the emerging magnification, having given proper consideration to the desired minimum value for the variable softening.

(12) We commend the algorithm for use in periodic N-body simulations from which the data can be manipulated to obtain emergent values from linked simulation cubes covering great distances. In this way, such a procedure also allows the comparison of results from different cosmologies. It is anticipated that our algorithm will become publicly available in enhanced form in due course.

ACKNOWLEDGMENTS

We are indebted to the facilities supported by NSERC in Canada, and to the Starlink minor node at the University of Sussex, for the preparation of this paper. We thank NATO for the award of a Collaborative Research Grant (CRG 970081), which has greatly facilitated our interaction. AJB is sponsored by the University of Sussex. HMPC thanks the Canadian Institute for Theoretical Astrophysics for hospitality during the academic year 1996/97. We have benefited also from valuable discussions with R. L. Webster and C. J. Fluke of the University of Melbourne, and K. Subramanian and D. Roberts whilst they visited the University of Sussex.

REFERENCES

Blandford R. D., Kochanek C. S., 1987, in Bahcall J. N., Piran T., Weinberg S., eds, Proc. 4th Jerusalem Winter School for Theoretical Physics, Dark Matter in the Universe. World Scientific, Singapore, p.133
Blandford R. D., Narayan R., 1986, ApJ, 310, 568
Couchman H. M. P., 1991, ApJ, 368, L23
Couchman H. M. P., Thomas P. A., Pearce F. R., 1995, ApJ, 452, 797
Dyer C. C., Roeder R. C., 1973, ApJ, 180, L31
Ewald P. P., 1921, Ann. Physik, 64, 253
Fluke C. J., Webster R. L., Mortlock D. J., 1998, preprint (astro-ph/9812300)
Gingold R. A., Monaghan J. J., 1977, MNRAS, 181, 375
Hockney R. W., Eastwood J. W., 1988, Computer Simulation Using Particles. IOP Publishing, ISBN 0-85274-392-0
Holz D. E., Wald R. M., 1998, Phys. Rev. D, 58, 63501
Jaroszyński M., Park C., Paczynski B., Gott III J. R., 1990, ApJ, 365, 22
Kovner I., 1987, ApJ, 316, 52

Marri S., Ferrara A., 1998, ApJ, 509, 43
Nijboer B. R. A., de Wette F. W., 1957, Physica, 23, 309
Peacock J. A., Dodds S. J., 1994, MNRAS, 267, 1020
Peebles P. J. E., 1993, Principles of Physical Cosmology. Princeton Univ. Press, Princeton, ISBN 1993 0-691-07428-3
Premadi P., Martel H., Matzner R., 1998, ApJ, 493, 10
Refsdal S., 1970, ApJ, 159, 357
Schneider P., Weiss A., 1988a, ApJ, 327, 526
Schneider P., Weiss A., 1988b, ApJ, 330, 1
Schneider P., Ehlers J., Falco E.E., 1992, Gravitational Lenses. Springer-Verlag, ISBN 0-387-97070-3
Tomita K., 1998a, preprint (astro-ph, 9806003)
Tomita K., 1998b, Prog. Theor. Phys., 100, 79
Vianna P. T. P., Liddle A. R., 1996, MNRAS, 281, 323
Wambsganss J., 1990, Thesis of Max-Planck-Institut Für Physik und Astrophysik, Ref. MPA, 550
Wambsganss J., Cen R., Xu G., Ostriker J. P., 1997, ApJ, 475, L81
Wambsganss J., Cen R., Ostriker J., 1998, ApJ, 494, 29

APPENDIX A: PERIODICITY AND THE PECULIAR POTENTIAL

A common method for modelling a section of the Universe is to consider a distribution of masses within a triply periodic cube. In this appendix we examine how the peculiar potential in this model relates to that in a universe with large-scale homogeneity.

A1 The peculiar potential

In Friedmann–Robertson–Walker models when considering the growth of perturbations, gravitational lensing by cosmic structure, etc., we are interested in deviations from homogeneity. The quantity of interest in this case is the *peculiar* potential. This is derived in the usual way by writing the equation of motion,

$$\frac{\mathrm{d}^2\boldsymbol{r}}{\mathrm{d}t^2} = -\nabla_{\mathbf{r}}\Phi, \tag{A1}$$

for matter at position $\boldsymbol{r}$, in terms of a comoving coordinate $\boldsymbol{r} = a\boldsymbol{x}$, where a is the expansion scalefactor. The peculiar potential – the source for deviations from homogeneity – is

$$\phi = \Phi + 1/2a\ddot{a}x^2. \tag{A2}$$

The rate of change of expansion velocity, $\ddot{a}$, is determined by the mean density of matter, $\bar{\rho}$, leading to the familiar results

$$\nabla^2\phi = 4\pi G a^2(\rho - \bar{\rho}) \tag{A3}$$

and

$$\phi = \Phi - 2/3\pi G a^2 \bar{\rho} x^2 \tag{A4}$$

(for full details see, e.g., Peebles 1993). The peculiar potential arising from Poisson's equation (A3) corresponds to a system with zero net mass on large scales.

Consider now a model universe of masses periodic in a cube of side L. The forces generated by the matter distribution satisfy $\boldsymbol{F}(\boldsymbol{x} + L\boldsymbol{n}) = \boldsymbol{F}(\boldsymbol{x})$, where $\boldsymbol{n}$ is an integer triple. Thus integrals, $\int_{L^2} \boldsymbol{F}\cdot\mathrm{d}\boldsymbol{S}$, where $\boldsymbol{S}$ is an outward normal, taken over opposite faces of the cube, sum to zero, and $\int_S \boldsymbol{F}\cdot\mathrm{d}\boldsymbol{S}$ over the surface of the cube vanishes. The divergence theorem and Poisson's equation, $\nabla^2\phi = 4\pi G\rho'$, then imply

$$4\pi G\int_{L^3}\rho'\mathrm{d}V = \int_{L^3}\nabla^2\phi\,\mathrm{d}V = -\int_{L^3}\nabla\cdot\boldsymbol{F}\,\mathrm{d}V = -\int_S \boldsymbol{F}\cdot\mathrm{d}\boldsymbol{S} = 0, \tag{A5}$$

and hence the total mass in the system is zero.

This result is a consequence of solving Poisson's equation in a periodic cube. We see that the real result for the shear, obtained from the second derivatives of the peculiar potential, ϕ, is related to the naïve result based on the full gravitational potential, Φ, through the use of $\rho' = \rho - \bar{\rho}$.

Note that the zero mean density implicit in equation (A3) is a result of the coordinate transformation; that this transformation is well motivated is a reflection of the large-scale homogeneity of the universe. The zero mean density in equation (A5), on the other hand, is simply a result of the imposed periodicity. The two views converge only for a periodic cube sufficiently large that the amplitude of the first few discrete Fourier modes are small enough that they describe a smooth transition to a zero mean value and homogeneity.

A2 The peculiar potential in a periodic system

We begin by demonstrating a useful result relating the Fourier transforms of continuous functions and the Fourier coefficients of the periodic functions constructed from them. First, as a convenient mechanism for translating between Fourier representations of continuous

and periodic functions, we define the three-dimensional comb $\amalg(x) = \sum_{\boldsymbol{n}} \delta(\boldsymbol{x} - \boldsymbol{n})$, where $\boldsymbol{n}$ is an integer triple (see, e.g., Hockney & Eastwood 1988). The Fourier transform of this function is the comb $\amalg(\boldsymbol{k}/2\pi)$.

Consider the function, with period L, constructed by periodically repeating f:

$$f^{\dagger}(\boldsymbol{x}) = \amalg\!\amalg\!\amalg(\boldsymbol{x}/L) * f(\boldsymbol{x}) \tag{A6}$$

$$= \sum_{\boldsymbol{n}} f(\boldsymbol{x} - \boldsymbol{n}L). \tag{A7}$$

Applying the Fourier convolution theorem to equation (A6), we see immediately that the Fourier transform of the periodic function, $f^{\dagger}$, is

$$\tilde{f}^{\dagger}_{\boldsymbol{k}} = \amalg\!\amalg\!\amalg\left(\frac{\boldsymbol{k}}{L/2\pi}\right)\tilde{f}(\boldsymbol{k}), \tag{A8}$$

where $\tilde{f}$ is the continuous Fourier transform of f.

Equation (A8) gives the Fourier series representation of the periodic function directly, and demonstrates the familiar result that the Fourier coefficients of the continuous periodic function, obtained by accumulating repeats of the continuous function (here $\sum_{\boldsymbol{n}} f(\boldsymbol{x} - \boldsymbol{n}L)$ obtained from f), are the same as the Fourier components of the continuous function at wavenumbers $\boldsymbol{k} = 2\pi\boldsymbol{l}/L$. This result is the analogue in real space of aliasing in Fourier space. If the continuous function is zero outside the fundamental cell, the periodic representation is simply obtained by tiling space with repeats of the fundamental cell. (This is the real-space analogue of a band-limited function.)

Consider now N particles distributed in a cube of side L. Let the position of particle i be $\boldsymbol{x}_i$. The density is then

$$\rho(\boldsymbol{x}) = \sum_j m_j \delta(\boldsymbol{x} - \boldsymbol{x}_j), \tag{A9}$$

without, for the moment, requiring zero total mass. Where necessary, we can consider a periodic density distribution constructed by tiling space with periodic repeats of the distribution in the fundamental cube:

$$\rho'(\boldsymbol{x}) = \amalg\!\amalg\!\amalg(\boldsymbol{x}/L) * \rho(\boldsymbol{x}). \tag{A10}$$

The gravitational potential at a point $\boldsymbol{x}$ in the periodic system is

$$\phi(\boldsymbol{x}) = G\amalg\!\amalg\!\amalg(\boldsymbol{x}/L) * \rho(\boldsymbol{x}) * \varphi(\boldsymbol{x}), \tag{A11}$$

where φ is the pairwise 'interaction' potential (or Green's function). Equation (A11) may be interpreted in two ways. We may consider a periodic distribution of matter as in equation (A10) convolved with the regular interaction potential. Alternatively, we can restrict attention to the matter in the fundamental zone and consider a modified interaction potential

$$\varphi^{\dagger}(\boldsymbol{x}) = \amalg\!\amalg\!\amalg(\boldsymbol{x}/L) * \varphi(\boldsymbol{x}) \tag{A12}$$

$$= \sum_{\boldsymbol{n}} \varphi(\boldsymbol{x} - \boldsymbol{n}L). \tag{A13}$$

Both of these interpretations will be useful.

Using the result in equation (A11), the Fourier series coefficients of ϕ are, for $\boldsymbol{k} = 2\pi\boldsymbol{l}/L$ and $\boldsymbol{l}$ an integer triple,

$$\tilde{\phi}_{\boldsymbol{k}} = G\tilde{\rho}(\boldsymbol{k})\tilde{\varphi}(\boldsymbol{k}), \tag{A14}$$

where $\tilde{\rho}(\boldsymbol{k}) = \sum_j m_j \mathrm{e}^{-\mathrm{i}\boldsymbol{k}\cdot\boldsymbol{x}_j}$ is the continuous Fourier transform of the particle distribution in the fundamental zone (equation (A9)) and $\tilde{\varphi}(\boldsymbol{k})$ is the continuous Fourier transform of the interaction potential.

Requiring the mean mass to be zero is equivalent to subtracting a component equal to $\sum_i m_i/L^3$ from the density in equation (A9), or setting $\tilde{\phi}_{\boldsymbol{k}=0} = 0$ in equation (A14). With this modification equation (A11) becomes

$$\phi(\boldsymbol{x}) = G\amalg\!\amalg\!\amalg(\boldsymbol{x}) * \sum_j m_j \left[\varphi(\boldsymbol{x} - \boldsymbol{x}_j) - \frac{1}{L^3}\int_{L^3} \varphi(\boldsymbol{x} - \boldsymbol{x}')\,\mathrm{d}^3\boldsymbol{x}'\right] \tag{A15}$$

$$= G\left[\sum_{j\boldsymbol{n}} m_j \varphi(\boldsymbol{x} - \boldsymbol{x}_{j\boldsymbol{n}}) - \frac{\sum_j m_j}{L^3}\sum_{\boldsymbol{n}}\int_{L^3} \varphi(\boldsymbol{x} - \boldsymbol{n}L - \boldsymbol{x}')\,\mathrm{d}^3\boldsymbol{x}'\right] \tag{A16}$$

$$= G\sum_j m_j \left[\sum_{\boldsymbol{n}} \varphi(\boldsymbol{x} - \boldsymbol{x}_{j\boldsymbol{n}}) - \frac{1}{L^3}\int \varphi(\boldsymbol{x}')\,\mathrm{d}^3\boldsymbol{x}'\right] \tag{A17}$$

$$= G\sum_{j\boldsymbol{n}} m_j \left[\varphi(\boldsymbol{x} - \boldsymbol{x}_{j\boldsymbol{n}}) - \frac{1}{L^3}\int_{L^3} \varphi(\boldsymbol{x}' - \boldsymbol{n}L)\,\mathrm{d}^3\boldsymbol{x}'\right], \tag{A18}$$

where $\boldsymbol{x}_{j\boldsymbol{n}} = \boldsymbol{x}_j + \boldsymbol{n}L$ and $j\boldsymbol{n}$ labels the image of the jth particle in the image cell $\boldsymbol{n}$. We may write equation (A18) as

$$\phi(\boldsymbol{x}) = G\rho(\boldsymbol{x}) * \varphi\dagger(\boldsymbol{x}), \tag{A19}$$

where we now have for the density

$$\rho(\boldsymbol{x}) = \sum_j m_j \left[\delta(\boldsymbol{x} - \boldsymbol{x}_j) - \frac{1}{L^3}\right], \tag{A20}$$

and equation (A13) is now

$$\varphi^{\dagger}(\boldsymbol{x}) = \sum_{\boldsymbol{n}} \left[\varphi(\boldsymbol{x} - \boldsymbol{n}L) - \frac{1}{L^3}\int_{L^3} \varphi(\boldsymbol{x}' - \boldsymbol{n}L)\,\mathrm{d}^3\boldsymbol{x}'\right]. \tag{A21}$$

It is unnecessary for the mean value of *both* ρ and φ to be zero. The form for the modified potential is convenient, however, since, for a potential which is Coulombic at large scales, with $\varphi \sim 1/r$, the form in equation (A21) is convergent, whereas the form in equation (A13) is not: nor does the integral in equation (A17) converge. The Fourier synthesis of the peculiar potential is

$$\phi(\boldsymbol{x}) = \frac{G}{L^3}\sum_{\boldsymbol{k}\neq 0} \mathrm{e}^{\mathrm{i}\boldsymbol{k}\cdot\boldsymbol{x}}\tilde{\rho}(\boldsymbol{k})\tilde{\varphi}(\boldsymbol{k}). \tag{A22}$$

A3 Particle softening

The delta function in equation (A9) may be replaced by any compact even function, with volume integral equal to unity, to represent a distribution of softened particles. (The softening will be considered fixed for the present to permit Fourier analysis.) However, since it is only the *interaction* of the particles via the gravitational field which is relevant, we may, equivalently, describe any particle softening by modifying the pairwise (Coulombic) potential, φ, at small separations.

From equation (A22) we can immediately write

$$\nabla^2\phi = -\frac{G}{L^3}\sum_{\boldsymbol{k}\neq 0} \mathrm{e}^{\mathrm{i}\boldsymbol{k}\cdot\boldsymbol{x}}\tilde{\rho}(\boldsymbol{k})k^2\tilde{\varphi}(\boldsymbol{k}). \tag{A23}$$

For a Coulombic interaction potential, $\varphi(r) = -1/r$, we have $\tilde{\varphi}(k) = -4\pi/k^2$. If we set $\tilde{\varphi}(k) = -4\pi\tilde{S}(k)/k^2$ with $\tilde{S}(0) = 1$, then $S(R)$ describes the departure of the interaction potential from Coulombic at small scales and, as we will see, plays the role of a particle softening. Equation (A23) becomes

$$\nabla^2\phi = \frac{4\pi G}{L^3}\sum_{\boldsymbol{k}\neq 0} \mathrm{e}^{\mathrm{i}\boldsymbol{k}\cdot\boldsymbol{x}}\tilde{\rho}(\boldsymbol{k})\tilde{S}(\boldsymbol{k}) \tag{A24}$$

$$= 4\pi G\rho(\boldsymbol{x}) * S(\boldsymbol{x}) \tag{A25}$$

$$= 4\pi G\rho_S \tag{A26}$$

which is Poisson's equation for a distribution of softened point charges;

$$\rho_S(\boldsymbol{x}) = 4\pi G\sum_j \left[S(\boldsymbol{x} - \boldsymbol{x}_j) - \frac{1}{L^3}\right]. \tag{A27}$$

Note that if we wanted the force on a softened particle from the distribution of softened particles (rather than merely sampling the density field at a point), the appropriate interaction potential in Fourier space would be $\tilde{\varphi} = -4\pi\tilde{S}^2(k)/k^2$.

APPENDIX B: EQUIVALENCE OF 2D AND 3D SHEAR CALCULATIONS

B1 General

It is frequently assumed that for the purposes of determining deflections and shearing of light a three-dimensional mass distribution may be represented by a plane projection of the density. In particular, many workers in the field of gravitational lensing treat cosmological N-body simulation cubes as collapsed planes. In this appendix we investigate this assumption and show under what conditions the result holds.

The result is approximate because of the need to apply the appropriate angular diameter distances at every deflection site (or evaluation position). In our derivation we assume that these factors are constant along the line of sight through the projected volume, whereas in practice they will vary slightly through the simulation volume. (The technique developed in this work applies the angular diameter distances at every evaluation position within each three-dimensional realization, and evaluates the shear components at many locations within each to enable a complete description of the shearing of a light ray during its travel through the simulation.)

We will show that computations based on two-dimensional (planar) projections of three-dimensional (periodic) simulations are adequate provided: (a) the mass distribution is periodic along the line of sight, and a single (full) period is included in the projection; (b) proper account is taken of the full transverse extent of matter, (which should normally be assumed to be periodic,

unless strong lensing by matter limited in extent is being considered); by ignoring this requirement, it is likely that the convergence of deflection angles and shear components to their limiting values will not be achieved; (c) the net zero mass requirement is adopted.

Consider the peculiar potential, $\phi(\boldsymbol{x})$, in a three-dimensional periodic system as given above in equation (A18):

$$\phi(\boldsymbol{x}) = G\sum_{j\boldsymbol{n}} m_j \left[\varphi(\boldsymbol{x}-\boldsymbol{x}_{j\boldsymbol{n}}) - \frac{1}{L^3}\int_{L^3}\varphi(\boldsymbol{x}'-\boldsymbol{n}L)\,\mathrm{d}^3\boldsymbol{x}'\right]. \tag{B1}$$

As discussed in Section A2, the integral in equation (B1) is finite and the sum over $\boldsymbol{n}$ converges. Although we will be considering derivatives of the potential – in which case the second, constant, term drops out – it is useful to have a rigorous convergent expression for the peculiar potential in a periodic system.

We are interested in obtaining the integrated shear along a line of sight over one period: $\int_L \partial^2\phi(\boldsymbol{x})/\partial x_i\partial x_j\,\mathrm{d}z$. We will begin by integrating the peculiar potential over one period: $\int_L \phi(\boldsymbol{x})\,\mathrm{d}z$.

In the following we will split vectors over three dimensions into a two-dimensional component perpendicular to the line of sight and a component along the line of sight, here taken to be in the z direction. A superscript asterisk is used to denote two-dimensional quantities, e.g., $\boldsymbol{x} = (\boldsymbol{x}^*, z)$. Then the two-dimensional potential is

$$\begin{aligned}
\phi^*(\boldsymbol{x}^*) &= \int_L \phi(\boldsymbol{x})\,\mathrm{d}z \\
&= G\sum_{j\boldsymbol{n}^*} m_j \sum_{\mathrm{s}}\left[\int_L \mathrm{d}z\varphi(\boldsymbol{x}^*-\boldsymbol{x}^*_{j\boldsymbol{n}^*}, z-z_{j\mathrm{s}}) - \frac{1}{L^2}\int_L\int_{L^2}\varphi(\boldsymbol{x}^{*\prime}-\boldsymbol{n}^*L, z'-sL)\,\mathrm{d}^2\boldsymbol{x}^{*\prime}\,\mathrm{d}z'\right] \\
&= G\sum_{j\boldsymbol{n}^*} m_j \left[\int \mathrm{d}z\varphi(\boldsymbol{x}^*-\boldsymbol{x}^*_{j\boldsymbol{n}^*}, z-z_j) - \frac{1}{L^2}\int\int_{L^2}\varphi(\boldsymbol{x}^{*\prime}-\boldsymbol{n}^*L, z)\,\mathrm{d}^2\boldsymbol{x}^{*\prime}\,\mathrm{d}z'\right] \\
&= G\sum_{j\boldsymbol{n}^*} m_j \left[\varphi^*(\boldsymbol{x}^*-*^*_{j\boldsymbol{n}^*}) - \frac{1}{L^2}\int_{L^2}\varphi^*(\boldsymbol{x}^{*\prime}-\boldsymbol{n}^*L)\,\mathrm{d}^2\boldsymbol{x}^{*\prime}\right],
\end{aligned} \tag{B2}$$

where

$$\varphi^*(\boldsymbol{x}^*) = \int \varphi(\boldsymbol{x}^*, z)\,\mathrm{d}z. \tag{B3}$$

Equation (B2) is the two-dimensional analogue of equation (B1), with the interaction potential, φ replaced by φ^*. Thus the three-dimensional peculiar potential integrated over one period L in one dimension, gives the same result as that obtained from the projected (surface) density of particles with a two-dimensional interaction potential arising from the projection from $-\infty$ to ∞ of the three-dimensional interaction potential. The corresponding results for the shear components, $\partial^2\phi^*/\partial x_i\partial x_j$, $x_i, x_j \neq z$, follow directly.

B2 Special case of a Coulombic potential

For the case of a Coulombic potential in three dimensions, $\varphi = -1/r$, where $r^2 = \boldsymbol{x}^{*2} + z^2$, $\varphi^*(\boldsymbol{x}^*) = -\int \mathrm{d}z/r$ diverges. Consider the two-dimensional potential over a finite range in z, $0 \le z \le M$,

$$\begin{aligned}
\varphi^*_M(\boldsymbol{x}^*) &= 2\int_0^M \varphi\,\mathrm{d}z \\
&= -2\int_0^M \frac{\mathrm{d}z}{\sqrt{\boldsymbol{x}^{*2}+z^2}} \\
&= 2\ln|\boldsymbol{x}^*| - 2\ln(M+\sqrt{\boldsymbol{x}^{*2}+M^2}).
\end{aligned} \tag{B4}$$

From equation (B2) we can then write

$$\begin{aligned}
\phi^*(\boldsymbol{x}^*) &= \lim_{M\to\infty}\left\{G\sum_{j\boldsymbol{n}} m_j\left[\varphi^*_M(\boldsymbol{x}^*-\boldsymbol{x}^*_{j\boldsymbol{n}^*}) - \frac{1}{L^2}\int_{L^2}\varphi^*_M(\boldsymbol{x}^{*\prime}-\boldsymbol{n}^{*\prime}L)\,\mathrm{d}^2\boldsymbol{x}^{*\prime}\right]\right\} \\
&= G\sum_{j\boldsymbol{n}} m_j\left[2\ln|\boldsymbol{x}^*-\boldsymbol{x}^*_{j\boldsymbol{n}^*}| - \frac{1}{L^2}\int_{L^2} 2\ln|\boldsymbol{x}^{*\prime}-\boldsymbol{n}^{*\prime}L|\,\mathrm{d}^2\boldsymbol{x}^{*\prime}\right].
\end{aligned} \tag{B5}$$

Thus, for $\varphi(r) = -1/r$, the appropriate two-dimensional potential is $\varphi^*(r^*) = 2\ln(r^*)$, as expected.

B3 Softening

The discussion above applies to any suitably well-behaved interaction potential, φ. In particular, consider the case of a distribution of softened particles. This may be described in terms of an interaction potential which is Coulombic at large scales but which falls below $1/r$ at small scales. It is most convenient to derive the appropriate φ^* in Fourier space. We may set $\tilde{\varphi}(k) = -4\pi\tilde{S}^2(k)/k^2$ with $\tilde{S}(0) = 1$ (see Section A3). The required two-dimensional Fourier transform is then

$$\tilde{\varphi}^*(k^*) = \int \mathrm{e}^{\mathrm{i}\boldsymbol{k}^*\cdot\boldsymbol{x}^*}\,\mathrm{d}^2\boldsymbol{x}^* \int \phi(\boldsymbol{x})\,\mathrm{d}z = \tilde{\phi}(\boldsymbol{k}^*, 0). \tag{B6}$$

Thus, for a given softening function S, the appropriate function φ^* may be found, although an analytic solution may not be possible especially in view of the notorious difficulty of two-dimensional Fourier integrals.

APPENDIX C: THE EWALD SUMMATION METHOD

In this appendix we turn to the numerical evaluation of sums for the potential and its derivatives in a periodic system such as those in equation (B1). For a Coulombic potential $\int \varphi(\boldsymbol{x})\,\mathrm{d}^3\boldsymbol{x}$ is divergent and the potential is well defined (and convergent) only if there is a uniform negative mass density to cancel the distribution of positive mass particles. Even if this condition is met, the sum for the potential is only slowly convergent and difficult to compute numerically. Ewald (1921) proposed a method for computing such sums in the context of calculating lattice potentials of ionic crystals. The electrostatic problem suffers from exactly the same numerical difficulties as the gravitational problem (the pairwise potential in each case is Coulombic), and it is well known that naïvely summing over images of the fundamental cell gives an order-dependent result. Note that the requirement for zero total mass is the same as the requirement in calculating crystal energies that the total charge be zero. We derive below Ewald's method as it is applied to the problem of computing the gravitational potential, and give expressions for the first and second derivatives of the potential – respectively the force and shear – and the total potential. We also demonstrate the relationship of the $\mathrm{P^3M}$ technique to the Ewald method.

C1 The Ewald method

Consider again a system of N particles in a cube of side L. The density is given by equation (A20):

$$\rho(\boldsymbol{x}) = \sum_j m_j \left[\delta(\boldsymbol{x} - \boldsymbol{x}_j) - \frac{1}{L^3}\right]. \tag{C1}$$

The second term on the right-hand side of equation (C1) makes the mean density zero, as required for the existence of a solution to Poisson's equation. As noted in Section A3, the delta function in equation (C1) may be replaced by any compact even function, with volume integral equal to unity, to represent a distribution of particles with fixed softening. Alternatively, and equivalently, the interaction potential may be suitably modified.

The gravitational potential at a point $\boldsymbol{x}$ within the cube is given by equation (A18):

$$\phi(\boldsymbol{x}) = G\sum_{j\boldsymbol{n}} m_j \left[\varphi(\boldsymbol{x} - \boldsymbol{x}_{j\boldsymbol{n}}) - \frac{1}{L^3}\int_{L^3} \varphi(\boldsymbol{x}' - \boldsymbol{n}L)\,\mathrm{d}^3\boldsymbol{x}'\right], \tag{C2}$$

where the notation is as in Section A2. Note that evaluating equation (C2) at a particle position, $\boldsymbol{x}_i$, will include the self-energy of particle i.

The sum in equation (C2) converges very slowly and is ill conditioned for numerical computation. Ewald (1921) proposed splitting the Coulombic potential into two components,

$$\varphi(R) = \varphi_1(R) + \varphi_2(R), \tag{C3}$$

where the functional form of the split is chosen so that the first component is dominated by quickly converging local contributions, and the second contains the relatively smooth long-range components of the field. The attenuation of high frequencies in the second component ensures rapid convergence of the corresponding sum when recast as a Fourier series. Ewald proposed taking $\varphi_1 = -\mathrm{erfc}(\eta R)/R$, $\varphi_2(R) = -1/R - \varphi_1(R) = -\mathrm{erf}(\eta R)/R$, where erf and erfc are the error and complementary error functions respectively. The parameter η is chosen to optimize convergence of the resulting real- and Fourier-space sums. For the moment we will not specify the functional form and will continue with the description in equation (C3).

If we ignore for the moment the mean contribution in equation (C2), we can write the potential as

$$\phi(\boldsymbol{x}) = G\sum_{j\boldsymbol{n}} m_j \varphi_1(\boldsymbol{x} - \boldsymbol{x}_{j\boldsymbol{n}}) + \frac{G}{L^3}\sum_{\boldsymbol{k}} \mathrm{e}^{\mathrm{i}\boldsymbol{k}\cdot\boldsymbol{x}}\tilde{\Phi}_{2\boldsymbol{k}}. \tag{C4}$$

The second term is a Fourier series sum over $\boldsymbol{k} = 2\pi\boldsymbol{l}/L$, $\boldsymbol{l}$ an integer triple, because of the periodicity of the system. Referring to the result in equation (A14), we see that the Fourier components $\tilde{\Phi}_{2\boldsymbol{k}}$ are given by

$$\tilde{\Phi}_{2\boldsymbol{k}} = \tilde{\rho}'(\boldsymbol{k})\tilde{\varphi}_2(\boldsymbol{k}), \tag{C5}$$

where $\rho'(\boldsymbol{x}) = \sum_j \delta(\boldsymbol{x} - \boldsymbol{x}_j)$. This is completely equivalent to the results of Section A2 but with $\tilde{\varphi}$ replaced by $\tilde{\varphi}_2$, the only difference being that there will be a much larger effective softening for φ_2.

We will now ensure that the mean density is zero. It is not sufficient simply to set $\tilde{\Phi}_{2,\boldsymbol{k}=0} = 0$ in equation (C4) as part of the mean value of the field is contained in the first (real-space) term. The required potential is

$$\phi(\boldsymbol{x}) = G\sum_{j\boldsymbol{n}} m_j \varphi_1(\boldsymbol{x} - \boldsymbol{x}_{j\boldsymbol{n}}) - \frac{G\sum_j m_j}{L^3}\tilde{\varphi}_1(\boldsymbol{k}=0) + \frac{G}{L^3}\sum_{\boldsymbol{k}\neq 0} \mathrm{e}^{\mathrm{i}\boldsymbol{k}\cdot\boldsymbol{x}}\tilde{\Phi}_{2\boldsymbol{k}}. \tag{C6}$$

The continuous Fourier transform of the potential in equation (C6) gives, after straightforward manipulation,

$$\tilde{\phi}(\boldsymbol{k}) = G\tilde{\varphi}(\boldsymbol{k})\left[\tilde{\rho}'(\boldsymbol{k}) - \sum_j m_j\delta(\boldsymbol{k})\right] = G\tilde{\varphi}(\boldsymbol{k})\tilde{\rho}(\boldsymbol{k}), \tag{C7}$$

and thus, as required, the potential is the convolution of the total density, ρ, with the interaction potential, φ. Of course, for $\varphi(R) = -1/R$, then $\tilde{\varphi}(k) = -4\pi/k^2$ and we recover Poisson's equation in Fourier space.

Substituting for $\tilde{\rho}'(k)$ in equation (C5) and then using the result for $\tilde{\Phi}_{2\boldsymbol{k}}$ in equation (C6) gives the final result:

$$\phi(\boldsymbol{x}) = G\sum_{j\boldsymbol{n}} m_j \varphi_1(\boldsymbol{x} - \boldsymbol{x}_{j\boldsymbol{n}}) - \frac{G\sum_j m_j}{L^3}\tilde{\varphi}_1(\boldsymbol{k}=0) + \frac{G}{L^3}\sum_{j,\boldsymbol{k}\neq 0} \mathrm{e}^{\mathrm{i}\boldsymbol{k}\cdot(\boldsymbol{x}-\boldsymbol{x}_j)} m_j\tilde{\varphi}_2(k). \tag{C8}$$

The potentials φ_1 and φ_2 can be chosen so that both sums in equation (C8) converge rapidly.

For a given split of φ in equation (C3), we can calculate $\tilde{\varphi}_2(k)$ and hence efficiently calculate the potential at a point for a given particle distribution. From the expression in equation (C8) we may also derive expressions with similar desirable convergence properties for derivatives of the potential, such as the force and tidal field at $\boldsymbol{x}$:

$$\frac{\partial^s\phi}{\partial x_{\mu_1}\partial x_{\mu_2}\ldots\partial x_{\mu_s}} = G\left[\sum_{j\boldsymbol{n}} m_j \left.\frac{\partial^s\varphi_1(r)}{\partial r_{\mu_1}\partial r_{\mu_2}\ldots\partial r_{\mu_s}}\right|_{\boldsymbol{r}=\boldsymbol{x}-\boldsymbol{x}_{j\boldsymbol{n}}} + \frac{1}{L^3}\sum_{j,\boldsymbol{k}\neq 0} i^s k_{\mu_1}k_{\mu_2}\ldots k_{\mu_s}\,\mathrm{e}^{\mathrm{i}\boldsymbol{k}\cdot(\boldsymbol{x}-\boldsymbol{x}_j)} m_j\tilde{\varphi}_2(k)\right]. \tag{C9}$$

For the first and second derivatives of $\varphi_1(r)$ we have $\partial\varphi_1/\partial r_\mu = (\varphi_1'/r)r_\mu$ and $\partial^2\varphi_1/\partial r_\mu\partial r_\nu = [(\varphi_1'/r)'/r]r_\mu r_\nu + (\varphi_1'/r)\delta_{\mu\nu}$. From equation (C9) we can immediately write

$$\nabla^2\phi = G\left[\sum_{j\boldsymbol{n}} m_j\nabla^2\varphi_1(\boldsymbol{x} - \boldsymbol{x}_{j\boldsymbol{n}}) - \frac{1}{L^3}\sum_{j,\boldsymbol{k}\neq 0} k^2\,\mathrm{e}^{\mathrm{i}\boldsymbol{k}\cdot(\boldsymbol{x}-\boldsymbol{x}_j)} m_j\tilde{\varphi}_2(k)\right]. \tag{C10}$$

We can recast the first term as a Fourier series, since it is periodic; as before, the coefficients for the Fourier sum are the same as those for the continuous transform. Using this result, we obtain

$$\nabla^2\phi = \frac{G}{L^3}\left[\sum_{j,\boldsymbol{k}} m_j\,\mathrm{e}^{\mathrm{i}\boldsymbol{k}\cdot(\boldsymbol{x}-\boldsymbol{x}_j)}\int \mathrm{e}^{-\mathrm{i}\boldsymbol{k}\cdot\boldsymbol{x}'}\nabla^2\varphi_1\,\mathrm{d}^3\boldsymbol{x}' - \sum_{j,\boldsymbol{k}\neq 0} k^2\,\mathrm{e}^{\mathrm{i}\boldsymbol{k}\cdot(\boldsymbol{x}-\boldsymbol{x}_j)} m_j\tilde{\varphi}_2(k)\right], \tag{C11}$$

where the integral is over all space. Note that the first sum includes the mean $\boldsymbol{k} = 0$ component. Equation (C11) leads directly to

$$\nabla^2\phi = -\frac{G}{L^3}\left\{\sum_{j,\boldsymbol{k}} \mathrm{e}^{\mathrm{i}\boldsymbol{k}\cdot(\boldsymbol{x}-\boldsymbol{x}_j)} m_j k^2\tilde{\varphi} - \lim_{k\to 0}[k^2\tilde{\varphi}_2(k)\sum_j m_j\right\}. \tag{C12}$$

If the interaction potential is Coulombic on large scales, $\varphi \sim -1/R$, then $\lim_{k\to 0} k^2\tilde{\varphi}_2 = -4\pi$, provided that $\varphi_1/\varphi_2 \to 0$ sufficiently rapidly with increasing R (this condition is satisfied for any practical splitting choice). Equation (C12) then gives

$$\nabla^2\phi = 4\pi G\rho, \tag{C13}$$

including the negative mean density as in equation (C1).

The total potential energy of the N particles in the box including interactions with all images is

$$U = \frac{G}{2}\sum_{\substack{i,j\boldsymbol{n}\\ j\boldsymbol{n}\neq i}} m_i m_j\varphi(\boldsymbol{x}_i - \boldsymbol{x}_{j\boldsymbol{n}}) \tag{C14}$$

(ignoring again temporarily the mean contribution to the peculiar potential in equation C2). We can make use of the same splitting in equation (C3) and the results that follow from it for the potential, provided that the condition $j \neq i$ is observed. This is straightforward to take into account in the real-space sum by directly omitting the terms $i = j$. The Fourier sum, however, expresses the long-range component as a field which, to be correct at all locations, must contain the contribution of particle i. Measuring the potential at $\boldsymbol{x}_i$ using equation (C4) will therefore include the self-energy of particle i arising from the interaction potential φ_2. The self-energy contribution from particle i to the Fourier sum is $Gm_i^2\varphi_2(R=0)/2$. Using equation (C8) we obtain, after a little manipulation, the result

$$U = \frac{G}{2}\left[\sum_{\substack{i,j\boldsymbol{n}\\ j\boldsymbol{n}\neq i}} m_i m_j\varphi_1(\boldsymbol{x}_i - \boldsymbol{x}_{j\boldsymbol{n}}) - \frac{\left(\sum_j m_j\right)^2}{L^3}\tilde{\varphi}_1(\boldsymbol{k}=0) + \frac{1}{L^3}\sum_{i,j,\boldsymbol{k}\neq 0} \mathrm{e}^{\mathrm{i}\boldsymbol{k}\cdot(\boldsymbol{x}_i-\boldsymbol{x}_j)} m_i m_j\tilde{\varphi}_2(k) - \sum_j m_j^2\varphi_2(R=0)\right]. \tag{C15}$$

C2 Practical issues in computing the Ewald sums

A number of choices are possible for the interaction splitting in equation (C3). Of primary interest is good convergence of both the real-space and Fourier-space sums. It is also important to choose splitting functions which allow an efficient numerical scheme to be constructed. The most commonly used is that given by Ewald (1921), but a number of others have been discussed in the literature (e.g. Nijboer & de Wette 1957).

The Ewald scheme is a one-parameter family with $\varphi_1(R) = -\mathrm{erfc}(\eta R)/R$, and $\varphi_2(R) = -\mathrm{erf}(\eta R)/R$. The Fourier transform (in three dimensions) of φ_2 is $\tilde{\varphi}_2(k) = -4\pi\,\mathrm{e}^{-k^2/(4\eta^2)}/k^2$. The parameter η is chosen to optimize convergence. Nijboer & de Wette (1957) show that both the real-space and Fourier-space series have the same rate of convergence if $\eta = \sqrt{\pi}/L$. Satisfactory results are obtained for a range of values near this result. Machine accuracy (32 bit) can typically be achieved with this value of η by extending the sums in real space and Fourier space to a radial distance of roughly five image cells or Fourier modes respectively. The analytic result is independent of the value of η although the rates of convergence of the sums are affected. Increasing η causes a faster convergence of the real-space sum, whilst requiring the accumulation of a greater number of terms in the Fourier series to achieve a given precision. If η deviates too much from the optimal value, one of the sums will require the accumulation of a large number of terms for good convergence, and we will be faced with the original computational problem which the splitting was introduced to solve.

Clearly, each computation of the potential (or force, etc.) requires O(N) operations, and so to find the force on each of N particles, for example, requires O(N^2) operations, and so is not competitive with other methods currently available. The present attraction of the method is its simplicity and that it enables forces to be calculated to high precision.

Some improvement in computational efficiency can be obtained by noting that the Fourier sums in equations (C8) and (C14) can be factorized. For equation (C8), for example, we can express $\sum_{j,\mathbf{k}\neq 0} \mathrm{e}^{\mathrm{i}\boldsymbol{k}\cdot(\boldsymbol{x}-\boldsymbol{x}_j)} m_j \tilde{\varphi}_2(k)$ as $\sum_{\mathbf{k}\neq 0} \mathrm{e}^{\mathrm{i}\boldsymbol{k}\cdot\boldsymbol{x}} \tilde{\varphi}_2(k)$ $(\sum_j m_j\,\mathrm{e}^{-\mathrm{i}\boldsymbol{k}\cdot\boldsymbol{x}_j})$. The sum over j can be pre-computed and stored for the small number of wavenumbers k required (typically a few hundred). This reduces the cost of the Fourier sum to an O(N) operation for a fixed number of wavemodes and allows the parameter η to be increased, which reduces the work of the real-space sum. Note that since φ_2 is a real, even function, its Fourier transform will also be real and even. This allows the complex exponential to be reduced to a cosine for numerical computation of the sum. (The factorization just described is then only marginally more complicated – see Section C4.)

C3 Relationship to the P^{3}M method

The P^{3}M algorithm uses an interaction splitting which can be described using the same terminology set out above. The splitting employed is analogous in many ways to choosing a very large value of η. This reduces the range over which the real-space sum must be accumulated and throws most of the work into the Fourier sum. In P^{3}M the real-space sum is reduced to such an extent that the effective range is much smaller than the periodic distance, L. Indeed, a different functional split is commonly used in which φ_1 is compact. This allows efficient techniques to be used in which only nearby particles need be included in the real-space sum. Since the effective range of the real-space sum is now much less than the period distance L, this part of the calculation now takes O(Nn) operations to compute, where n is the mean number of particles within the range of the function φ_1. Provided n does not become too large (as it unfortunately will in gravitational simulations as clustering develops), the real-space work is essentially O(N). Pushing much of the work into the Fourier domain is advantageous only if efficient methods are available for accumulating the Fourier sum and if we can avoid the convergence problems discussed above in accumulating forces from the Fourier components.

The Fourier part of the P^{3}M method is best understood in terms of equation (C6) rather than equation (C8). The key to the method lies in approximating the Fourier components $\tilde{\Phi}_{2\boldsymbol{k}}$. Instead of calculating afresh the Fourier sum for each value of $\boldsymbol{x}$ for which it is required, the result is interpolated from stored values discretized on a regular grid. Provided the field is adequately sampled, the error in this procedure can be reduced to acceptable levels. The interaction splitting must be chosen such that the number of grid points available is sufficient to represent the harmonic content of the field. Since the number of wavenumbers over which the field must be known may now be very large (a consequence of the short range of the real-space sum), an efficient method for calculating the Fourier components from the density field and interaction potential must be used. This is achieved by sampling the density field with a uniform grid and using a FFT technique for obtaining the potential. Using an FFT also ensures well-determined convergence properties for the Fourier sums.

C4 Formulæ for the Ewald method

Using the splitting described by Ewald, we will now write down explicit expressions for equations (C8) and (C14), which can be used to compute the potential, its derivatives and the total potential.

We have $\varphi_1 = -\mathrm{erfc}(\eta R)/R$, $\varphi_2 = -\mathrm{erf}(\eta R)/R$ and $\tilde{\varphi}_2 = -4\pi\,\mathrm{e}^{-k^2/(4\eta^2)}/k^2$. [The error function, erf(x), is $(2/\sqrt{\pi})\int_0^x \mathrm{e}^{-t^2}\,\mathrm{d}t$. Many approximations to erfc suitable for efficient numerical computation exist in the literature and are often also available in mathematical libraries on many current computers.] To calculate $\tilde{\varphi}_1(0)$, we must take the limit of the transform of $-1/R + \mathrm{erfc}(\eta R)/R$ as $k \to 0$. This gives $\tilde{\varphi}_1(0) = -\pi/\eta^2$. The value of $\varphi_2(0) = -\lim_{R\to 0}\mathrm{erf}(\eta R)/R = -2\eta/\sqrt{\pi}$. Recall that the Fourier modes are labelled by $\boldsymbol{k} = 2\pi\boldsymbol{l}/L$, where $\boldsymbol{l}$ is an integer triple. Finally, define $C(\boldsymbol{l}) = \sum_j m_j \cos(2\pi\boldsymbol{l}\cdot\boldsymbol{x}_j/L)$ and $S(\boldsymbol{l}) = \sum_j m_j \sin(2\pi\boldsymbol{l}\cdot\boldsymbol{x}_j/L)$. Putting all of this together, we find:

$$\phi(\boldsymbol{x}) = -G\left\{\sum_{j\boldsymbol{n}} m_j\,\mathrm{erfc}(\eta r)/r\Big|_{\boldsymbol{r}=\boldsymbol{x}-\boldsymbol{x}_{j\boldsymbol{n}}} - \frac{\pi\sum_j m_j}{\eta^2 L^3} + \frac{1}{\pi L}\sum_{\boldsymbol{l}\neq 0}\frac{1}{l^2}\left[C(\boldsymbol{l})\cos(2\pi\boldsymbol{l}\cdot\boldsymbol{x}/L) + S(\boldsymbol{l})\sin(2\pi\boldsymbol{l}\cdot\boldsymbol{x}/L)\right]\mathrm{e}^{-\pi^2 l^2/(L^2\eta^2)}\right\}, \tag{C16}$$

and

$$U = -\frac{G}{2}\left\{\sum_{\substack{i,jn\\ jn\neq i}} m_i m_j \,\mathrm{erfc}(\eta r)/r\Big|_{\boldsymbol{r}=\boldsymbol{x}_i-\boldsymbol{x}_{jn}} - \frac{\pi\left(\sum_j m_j\right)^2}{\eta^2 L^3} + \frac{1}{\pi L}\sum_{\boldsymbol{l}\neq 0}\frac{1}{l^2}[C^2(\boldsymbol{l})+S^2(\boldsymbol{l})]\,\mathrm{e}^{-\pi^2 l^2/(L^2\eta^2)} - \frac{2\eta}{\sqrt{\pi}}\sum\nolimits_j m_j^2\right\}. \tag{C17}$$

Derivatives of ϕ may be calculated trivially from equation (C16). We have:

$$\frac{\partial\phi}{\partial x_\mu} = G\left\{\sum_{jn} m_j\left[\mathrm{erfc}(\eta r) + \frac{2}{\sqrt{\pi}}\eta r\,\mathrm{e}^{-\eta^2 r^2}\right]\frac{r_\mu}{r^3}\Big|_{\boldsymbol{r}=\boldsymbol{x}-\boldsymbol{x}_{jn}} + \frac{2}{L^2}\sum_{\boldsymbol{l}\neq 0}\frac{l_\mu}{l^2}[C(\boldsymbol{l})\sin(2\pi\boldsymbol{l}\cdot\boldsymbol{x}/L) - S(\boldsymbol{l})\cos(2\pi\boldsymbol{l}\cdot\boldsymbol{x}/L)]\mathrm{e}^{-\pi^2 l^2/(L^2\eta^2)}\right\}, \tag{C18}$$

and

$$\frac{\partial^2\phi}{\partial x_\mu\partial x_\nu} = G\left\{\sum_{jn} m_j\left[-\frac{4}{\sqrt{\pi}}\eta^3\,\mathrm{e}^{-\eta^2 r^2}\frac{r_\mu r_\nu}{r^2} + \left(\mathrm{erfc}(\eta r) + \frac{2}{\sqrt{\pi}}\eta r\,\mathrm{e}^{-\eta^2 r^2}\right)\left(\frac{\delta_{\mu\nu}}{r^3} - 3\frac{r_\mu r_\nu}{r^5}\right)\right]_{\boldsymbol{r}=\boldsymbol{x}-\boldsymbol{x}_{jn}}\right.$$
$$\left. + \frac{4\pi}{L^3}\sum_{\boldsymbol{l}\neq 0}\frac{l_\mu l_\nu}{l^2}[C(\boldsymbol{l})\cos(2\pi\boldsymbol{l}\cdot\boldsymbol{x}/L) + S(\boldsymbol{l})\sin(2\pi\boldsymbol{l}\cdot\boldsymbol{x}/L)]\,\mathrm{e}^{-\pi^2 l^2/(L^2\eta^2)}\right\}. \tag{C19}$$

Note: asymptotically $\mathrm{erfc}(x) \sim 1/(\sqrt{\pi}x)\,\mathrm{e}^{-x^2}$.

This paper has been typeset from a TEX/LATEX file prepared by the author.